

# DynFaceRestore: Balancing Fidelity and Quality in Diffusion-Guided Blind Face Restoration with Dynamic Blur-Level Mapping and Guidance

Huu-Phu Do<sup>1\*</sup>, Yu-Wei Chen<sup>1\*</sup>, Yi-Cheng Liao<sup>1</sup>, Chi-Wei Hsiao<sup>2</sup>,  
Han-Yang Wang<sup>2</sup>, Wei-Chen Chiu<sup>1</sup>, Ching-Chun Huang<sup>1†</sup>

<sup>1</sup>National Yang Ming Chiao Tung University, Taiwan

<sup>2</sup>MediaTek Inc., Taiwan

## Abstract

*Blind Face Restoration aims to recover high-fidelity, detail-rich facial images from unknown degraded inputs, presenting significant challenges in preserving both identity and detail. Pre-trained diffusion models have been increasingly used as image priors to generate fine details. Still, existing methods often use fixed diffusion sampling timesteps and a global guidance scale, assuming uniform degradation. This limitation and potentially imperfect degradation kernel estimation frequently lead to under- or over-diffusion, resulting in an imbalance between fidelity and quality. We propose DynFaceRestore, a novel blind face restoration approach that learns to map any blindly degraded input to Gaussian blurry images. By leveraging these blurry images and their respective Gaussian kernels, we dynamically select the starting timesteps for each blurry image and apply closed-form guidance during the diffusion sampling process to maintain fidelity. Additionally, we introduce a dynamic guidance scaling adjuster that modulates the guidance strength across local regions, enhancing detail generation in complex areas while preserving structural fidelity in contours. This strategy effectively balances the trade-off between fidelity and quality. DynFaceRestore achieves state-of-the-art performance in both quantitative and qualitative evaluations, demonstrating robustness and effectiveness in blind face restoration.*

## 1. Introduction

Blind face restoration (BFR) involves recovering high-fidelity, detail-rich facial images from degraded inputs with unknown kernels [24, 34]. The main difficulty lies in enhancing facial details while preserving the individual’s identity, as shown in Fig. 1. Although GAN-based approaches [1, 22, 40] are effective at adding fine details, they

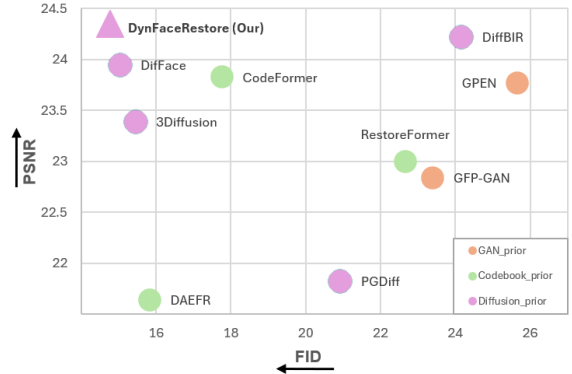


Figure 1. Blind face restoration demands both high fidelity and rich detail. Compared to other SOTA methods that leverage GAN priors, codebook priors, or diffusion priors, our proposed method, DynFaceRestore (denoted as an asterisk), demonstrates superior image fidelity (PSNR $\uparrow$ ) and quality (FID $\downarrow$ ) on the CelebA-Test.

often introduce artifacts. Recently, diffusion models (DM) [13] have demonstrated great generative capabilities to create more realistic details. However, DMs can still compromise fidelity in the restored faces.

Previous approaches [10, 38, 41] have effectively demonstrated the use of pre-trained diffusion models (DM) with high-quality (HQ) image priors to generate realistic facial details. Typically, [38, 41] apply DM for fine detail enhancement after mitigating degradation and recovering the structural information of low-quality (LQ) images using a restoration model. Meanwhile, [5, 10] aims to maintain image structures by guiding the DM through the measurement model. Despite these advancements, these methods still face challenges in maintaining fidelity. Below, we outline possible reasons for this limitation.

First, these methods assume that all LQ inputs exhibit uniform degradation severity and thus use a fixed starting timestep for diffusion sampling in image restoration. This approach often results in under- or over-diffusion when the DM adds details, as illustrated in Fig. 2. Sec-

\*Equal contribution

†Corresponding author, Ching-Chun Huang (chingchun@nycu.edu.tw)

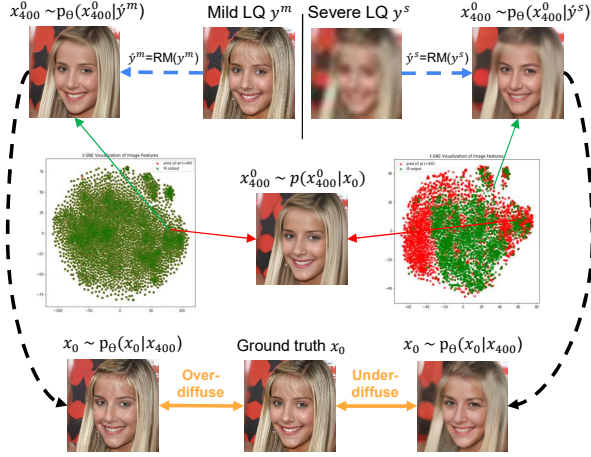


Figure 2. Using DiffFace [41] as an example, let  $RM$  represent DiffFace’s restoration model and  $p_\Theta$  the diffusion model. In the t-SNE plot, green and red points denote the features of  $x_{400}^0$  sampled from  $p_\Theta(x_{400}^0|y^m)$  and  $p_\Theta(x_{400}^0|x_0)$ , respectively. Here,  $y$ , the LQ image restored by  $RM$ , is used for diffusion guidance. DiffFace initiates the diffusion process at a fixed  $t = 400$ , resulting in under-diffusion (right) for severely degraded LQ images and just enough diffusion for mildly degraded LQ images (left). This underscores the importance of selecting an appropriate starting step.

ond, in blind settings, imperfect kernel estimation and arbitrary kernel forms frequently cause kernel mismatch issues, which misguide the diffusion sampling process. Third, high-frequency regions like hair and wrinkles benefit from stronger DM influence to enhance perceptual quality. In contrast, low-frequency regions, like facial contours, require greater guidance from the observed image to preserve fidelity. However, existing methods [5, 10, 38] that incorporate guidance into DM generally apply a uniform scale factor across all pixels, overlooking region-specific variations. This lack of localized adjustment can lead to suboptimal perceptual quality or fidelity loss, hindering the balance between detail enhancement and structural integrity.

In this paper, we introduce DynFaceRestore, which leverages a pre-trained diffusion model to enhance fine details while preserving fidelity through multiple Dynamic Blur-Level Mapping and Guidance. First, we design a discriminative restoration network that maps a blindly degraded input image into multiple Gaussian-blurred versions with estimated blur levels, effectively transforming unknown, variable degradation into a Gaussian form. Since perfect kernel estimation is often impractical, using multiple Gaussian-blurred images as multi-guidance for DM sampling helps address kernel mismatch issues. Second, the estimated blur level determines a dynamic starting timestep for each Gaussian-blurred image, ensuring optimal guidance insertion during diffusion and effectively addressing under- and over-diffusion challenges. Third, to enable

localized adjustment, we implement DPS-based guidance [4, 5] and introduce a novel dynamic guidance scale adjuster that adapts the guidance scale region-wise, resulting in high-fidelity, detail-rich outputs, as illustrated in Fig. 1. Our main contributions are summarized as follows:

- We introduce Dynamic Blur-Level Mapping and Guidance to address kernel mismatch issues effectively, using multi-level Gaussian-blurred images as guidance.
- Leveraging the estimated blur level from the restoration network output, we dynamically determine the optimal starting step in the diffusion process to prevent under- and over-diffusion.
- We construct a dynamic guidance scale adjuster to tailor the guidance strength across regions, harnessing the powerful influence of DM to improve perceptual quality while maintaining fidelity.
- Our proposed method, DynFaceRestore, outperforms state-of-the-art approaches in both quantitative and qualitative evaluations, demonstrating its superiority in Blind Face Restoration.

## 2. Related Works

### 2.1. Blind Face Restoration (BFR) with Priors

Previous BFR methods have utilized various priors to enhance restoration accuracy. Geometric prior methods [1, 2, 30] rely on structural data, such as landmarks and parsing maps, but often struggle when degraded inputs lack structural details. Reference prior methods [11, 33, 36, 43] use high-quality (HQ) reference images or codebooks. For example, VQ-GAN [9] provides detailed facial features; however, its fixed codebook size can limit the diversity and richness of restored faces. GAN-based approaches, such as PSFRGAN [1], incorporate facial parsing maps for style control, while models like GFP-GAN [22] and GPEN [40] focus on restoring facial fidelity by embedding pre-trained face models [18, 19]. Although GAN-based methods enhance face restoration quality, they often introduce artifacts.

Recently, diffusion-based approaches for BFR have achieved SOTA performance by either training a DM from scratch [3, 27–29, 32] or guiding a pre-trained DM [26, 37, 38, 41] to provide priors. For example, WaveFace [28] employs a conditional DM to generate high-frequency components, while 3Diffusion [27] integrates 3D facial structure into the noise estimation process. However, these methods typically require extensive training resources.

Other approaches leverage pre-trained diffusion models for restoration. DR2 [37] removes degradation using a pre-trained DM and enhances resolution via a super-resolution module. DiffBIR [26] employs a restoration module to remove degradation and regenerates details using a conditional pre-trained DM with ControlNet. DiffFace [41] maps a LQ input to an intermediate diffusion sampling step, then



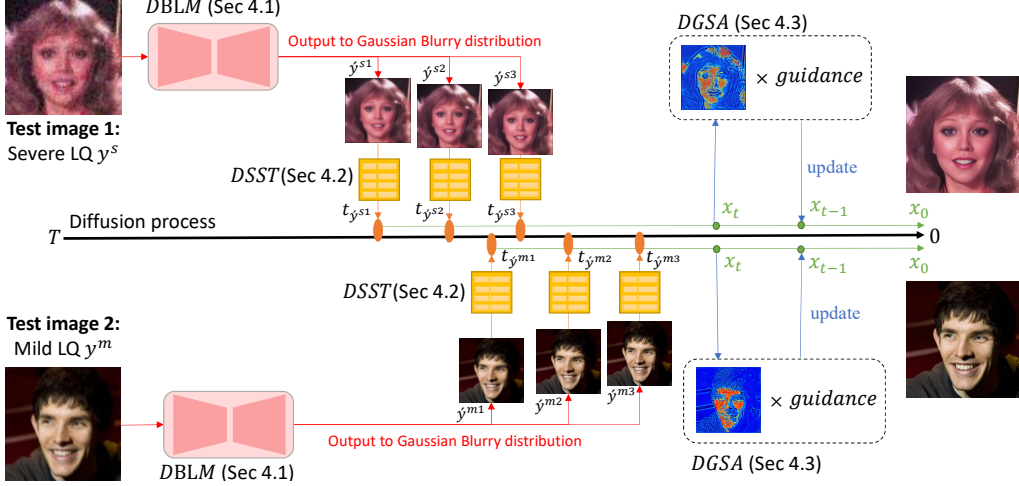


Figure 3. Overview of our proposed DynFaceRestore framework, which consists of three key components: DBLM, DSST, and DGSA (defined in Sec. 4). The upper and lower sections illustrate two independent restoration scenarios with inputs degraded to varying levels. DBLM generates multiple Gaussian-blurred images based on the degradation level of the unknown degraded input. Then, given these blur levels, DSST identifies the optimal starting step for each Gaussian-blurred image via a predefined lookup table, providing sampling guidance to avoid under- or over-diffusion. Lastly, the trained network, DGSA, locally adjusts the guidance scale used in the pre-trained diffusion process, enabling DynFaceRestore to achieve an optimal balance between fidelity and quality.

applies the standard DM backward process for restoration without extra guidance. In contrast, PGDiff [38] adopts classifier guidance to constrain the denoising process.

However, many of these DM-based methods overlook local degradation severity and rely on a fixed diffusion starting step, leading to suboptimal restoration. Recently, [26] addressed this issue by applying the Sobel operator on the LR image to set local guidance levels and introduce varying priors from DM. Yet, it struggles to capture intricate textures, as it focuses on local intensity without understanding global structures. In contrast, our proposed method provides “step-wise and region-specific guidance”, effectively adapting to both local and global features to preserve complex textures, as further discussed in Sec. 4.3.

## 2.2. Guidance on unconditional DM

Methods such as DDRM [20], DDNM [35], BlindDPS [5], Fast-diffusion EM [23], and GDP [10] avoid the need for restoration training by leveraging a pre-trained diffusion model. These approaches modify the intermediate output at each diffusion step to align with the degraded input (LQ image) as guidance. The alignment relies on a degradation model, represented by either a fixed linear matrix [20, 35], a kernel-based DM [5], or a learnable degradation model [10]. However, these methods generally assume a simple or linear degradation process, creating a significant domain gap when applied to complex real-world degradations. Additionally, they overlook kernel mismatch issues during diffusion, where the estimated kernel often deviates from the true degradation.

## 3. Preliminary and Framework Overview

### 3.1. Diffusion Posterior Sampling (DPS)

Consider the following observation model:

$$y = \mathcal{A}(x) + n, \quad (1)$$

where  $y$  is the measurement degraded from its HQ image counterpart  $x$ ,  $\mathcal{A}$  models the degradation process, and  $n$  is Gaussian noise. Based on Bayes’ rule, our goal is to sample or recover  $x$  from the posterior distribution  $p(x|y) \propto P(y|x)P(x)$ . Here, the likelihood  $P(y|x)$  is defined according to Eq. (1). When using a pre-trained DM to model the HQ image prior, the diffusion sampling process with  $y$  as guidance at timestep  $t$  can be expressed as

$$x_{t-1} = x'_{t-1} - s \nabla_{x_t} \log p_t(y|x_t), \quad (2)$$

where  $s$  is the guidance scale,  $x'_{t-1}$  is sampled from  $p(x_{t-1}|x_t)$ , and  $p_t(y|x_t)$  is likelihood.

Diffusion Posterior Sampling [4] builds upon a pre-trained DM from the Denoising Diffusion Probabilistic Model (DDPM) [13] and approximates the gradient of the likelihood  $\nabla_{x_t} \log p_t(y|x_t)$  as  $\nabla_{x_t} \log p_t(y|\hat{x}_t^0)$ , where

$$\hat{x}_t^0 = \frac{1}{\sqrt{\bar{\alpha}_t}}(x_t - \sqrt{1 - \bar{\alpha}_t}\epsilon_\theta). \quad (3)$$

Here,  $\epsilon_\theta$  is a learnable network used to define a diffusion model and  $\bar{\alpha}_t$  represents the pre-defined DDPM coefficients [13]. Based on Eq. (3) and using  $\epsilon_\theta$ , we can estimate the HQ

image  $\hat{x}_t^0$  from the diffusion sample  $x_t$ . Since  $\hat{x}_t^0 \cong x$ , we can utilize the observation model in Eq. (1) to replace the sample guidance in Eq. (2) as follows:

$$\nabla_{x_t} \log p_t(y|x_t) \approx \nabla_{x_t} \|y - \mathcal{A}(x_t^0)\|_2^2. \quad (4)$$

Note that  $\mathcal{A}$  should be given in advance. If  $\mathcal{A}$  is unknown or imperfectly estimated [5], an estimator or refiner for  $\mathcal{A}$  is necessary. Below, we proposed modifications to DPS and the way to refine  $\mathcal{A}$  during diffusion sampling.

### 3.2. DynFaceRestore Sampling

Rather than directly tackling the challenging BFR task, our DynFaceRestore method reframes it as a Gaussian deblurring problem by transforming the blindly degraded input image  $y$  into a Gaussian-blurred version  $\hat{y}$  and applying a modified DPS-based guidance for restoration. This allows us to represent  $\mathcal{A}(x_t^0)$  as  $k_t \otimes x_t^0$ , where  $k$  is a Gaussian blur kernel with standard deviation  $std$ . Consequently, our guided diffusion sampling process can be reformulated as follows:

$$x_{t-1} = x'_{t-1} - s \nabla_{x_t} \|\hat{y} - k_t \otimes x_t^0\|_2^2. \quad (5)$$

where  $x'_{t-1}$  sampled from  $p(x_{t-1}|x_t)$  is defined as follows:

$$x'_{t-1} = \frac{1}{\sqrt{\alpha_t}} (x_t - \frac{\beta_t}{\sqrt{1-\alpha_t}} \epsilon_\theta) + \sigma_t \epsilon, \epsilon \sim N(0, 1), \quad (6)$$

which are derived from diffusion model. However, perfect kernel estimation is often impractical; to reduce kernel mismatch, we also refine the  $\mathcal{A}$  during diffusion sampling. Since our  $\mathcal{A}$  is strictly a Gaussian blur kernel, we only need to update the estimated  $std$  by using the following equation.

$$std_{t-1} = std_t - s \nabla_{std_t} \|\hat{y} - k_t \otimes x_t^0\|_2^2. \quad (7)$$

Additionally, as shown in Fig. 3, the DynFaceRestore framework enhances DPS in the following four key aspects.

1. The DBLM (Sec. 4.1) first transforms a blindly degraded LQ input  $y$  into the corresponding Gaussian-blurred version  $\hat{y}$ , with blur levels adapted to the input's degradation level, enabling the representation of  $\mathcal{A}(x_t^0)$  as  $k_t \otimes x_t^0$ .
2. Then, through DSST table (Sec. 4.2), the optimal starting timestep  $t_{start}$  for diffusion is identified by using the estimated kernel (i.e.,  $\hat{std}^*$  in Sec. 4.1.1) as query. A right starting timestep would mitigate the effects of under- and over-diffusion. Next,  $\hat{y}$ ,  $\hat{std}^*$ , and  $t_{start}$  are used to initialize our DPS-based sampling process.
3. Instead of using a global scale  $s$ , during the sampling process, the DGSA (Sec. 4.3) dynamic adjusts guidance scale region-wise, balancing the restoration result's quality and fidelity.
4. Finally, we extend our framework to incorporate multiple guidance for the BFR task, as detailed in Sec. 4.4.

To better understand our work, we also outline the inference steps in Algorithm 1 for the reference.

---

#### Algorithm 1 Inference

---

**Require:**  $y$ : Unknown degraded LQ input;

**Ensure:**  $x_0$ : HQ sampled image;

- 1:  $\hat{y}, \hat{std}^* = DBLM(y), SE(y)$ ;
  - 2: compute Gaussian blur kernel  $k$  using  $\hat{std}^*$
  - 3:  $t_{start} = DSST(\hat{std}^*)$ ;
  - 4:  $x_{t_{start}} = \sqrt{\alpha_{t_{start}}} \hat{y} + \sqrt{1 - \alpha_{t_{start}}} \epsilon, \epsilon \sim N(0, 1)$ ;
  - 5:  $std_{t_{start}} = \hat{std}^*$ ;
  - 6: **for**  $t = t_{start} \cdots 1$  **do**
  - 7:  $x_t^0 = \frac{1}{\sqrt{\alpha_t}} x_t - \sqrt{\frac{1-\alpha_t}{\alpha_t}} \epsilon_\theta$ ;
  - 8:  $x'_{t-1} = \frac{1}{\sqrt{\alpha_t}} (x_t - \frac{\beta_t}{\sqrt{1-\alpha_t}} \epsilon_\theta) + \sigma_t \epsilon, \epsilon \sim N(0, 1)$ ;
  - 9: compute Gaussian blur kernel  $k_t$  using  $std_t$ ;
  - 10:  $A_t = DGSA(\hat{y}, x_t^0, t)$ ;
  - 11:  $x_{t-1} = x'_{t-1} - A_t \times \nabla_{x_t} \|\hat{y} - k_t \otimes x_t^0\|_2^2$ ;
  - 12:  $std_{t-1} = std_t - \sqrt{\alpha_t} \times \nabla_{k_t} \|\hat{y} - k_t \otimes x_t^0\|_2^2$ ;
  - 13: **end for**
  - 14: **return**  $x_0$
- 

## 4. Method

### 4.1. Dynamic Blur-Level Mapping

To leverage the reliable information (i.e., low-frequency components) of the degraded input and mitigate kernel mismatch issues during the diffusion process, we designed DBLM to first transform the degraded input  $y$  into a Gaussian-blurred counterpart  $\hat{y}$ , effectively converting blind kernel to a Gaussian form. Next,  $\hat{y}$  serves as a restored version of  $y$ , with maximally enhanced high-frequency details while preserving fidelity. Specifically, the DBLM function is defined as follows:

$$\hat{y} = DBLM(y) = k_y^{std^*} \otimes RM(y), \quad (8)$$

where  $RM$  represents any state-of-the-art discriminative image restoration model, with SwinIR [25] used in our implementation (details and other RMs' comparisons are defined in the Supplementary);  $k_y^{std^*}$ , parameterized by  $std^*$ , is the optimal Gaussian kernel related to the degradation level of  $y$ , where kernel standard  $std^*$  is determined by

$$\begin{aligned} std^* &\equiv \arg \min_{std \in [std_{min}, std_{max}]} (std), \\ \text{s.t. } &\|k^{std} \otimes RM(y) - k^{std} \otimes x\|_1 < \xi. \end{aligned} \quad (9)$$

In Eq. (19),  $\xi$  denotes the chosen error tolerance,  $x$  is the HQ ground truth, and  $\otimes$  represents the convolution operation. Ideally, Eq. (19) suggests that  $\tilde{x} \equiv k_y^{std^*} \otimes x$  is the amount of information recoverable from  $y$  by DBLM (as per Eq. (8)) with fidelity. Moreover, since  $\hat{y}$  the output of DBLM is explicitly degraded by the Gaussian kernel  $k_y^{std^*}$ , utilizing  $\hat{y}$  and  $k_y^{std^*}$  as guidance within our diffusion-based restoration framework (Sec. 3.2) mitigates the impact of kernel mismatch issues caused by inaccurate kernel predic-

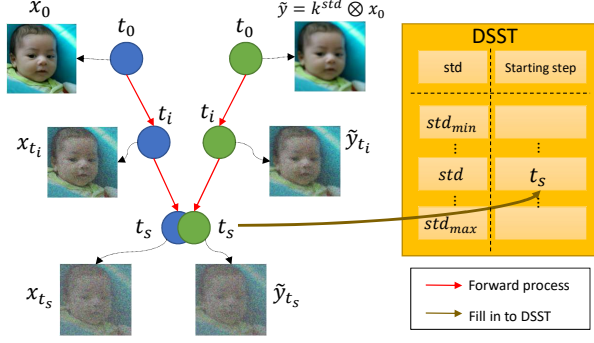


Figure 4. As  $t$  increases, the diffused  $x_t$  from HQ image  $x_0$  and the diffused  $\tilde{y}_t$  from the Gaussian-blurred image  $\tilde{y}$  gradually approach and converge at  $t_s$ . We leverage this property to form the basis for establishing DSST.

tions. However, the estimation of  $std^*$  merits further discussion during inference.

#### 4.1.1. Estimation of $std^*$

During inference, the ground truth  $x$  is unavailable, necessitating an alternative approach for estimating  $std^*$  instead of using Eq. (19). To achieve this, we design a learnable network (SE) to generate an estimate  $\hat{std}^*$  from the input  $y$ . SE first produces an intermediate output  $\hat{y}'$  that approximates  $\tilde{x}$ , and then, based on  $\hat{y}'$  derives  $\hat{std}^*$ . In summary,  $[\hat{std}^*, \hat{y}'] = SE(y)$ . The training objective function for SE is defined as follows:

$$L_{SE} = \mathbb{D}(\hat{std}^*, std^*) + \gamma_{std} \mathbb{D}(\hat{y}', \tilde{x}), \quad (10)$$

where  $\mathbb{D}$  is the L1 distance and  $\gamma_{std}$  is a weighting factor for balancing. Additionally,  $std^*$  and  $\tilde{x}$  are the training labels derived from Sec. 4.1. Note that  $\hat{y}'$ , predicted by the SE, maps the unknown degraded input image  $y$  to an intermediate blurred version, serving as an alternative to the Gaussian-blurred counterpart  $\tilde{y}$  from Eq. (8). However,  $\hat{y}'$  does not perfectly conform to the assumed Gaussian form and is unsuitable as Gaussian-blurred guidance in the subsequent diffusion sampling process. Thus, in our final implementation, we use  $\tilde{y}$  instead of  $\hat{y}'$ , estimating  $\tilde{y}$  via Eq. (8), with  $\hat{std}^*$  replaced by  $std^*$ . Due to space constraints, a detailed analysis of the differences between  $\tilde{y}$  and  $\hat{y}'$ , along with the design details of the SE, is provided in the Supplementary.

## 4.2. Dynamic Starting Step Lookup Table

Based on the estimated blur level,  $std^*$ , we develop a strategy to determine the starting timesteps for inserting guidance  $\tilde{y}$  into DM to prevent under- and over-diffusion. The idea is illustrated in Fig. 4. Assume  $x_0 \equiv x$  represents

an HQ image and  $\tilde{y}_0^{std} = k^{std} \otimes x$  is its blurred counterpart. When both images undergo the same forward degradation process defined in a standard diffusion model, they will statistically converge after a specific timestep  $t$ , meaning  $x_t \cong \tilde{y}_t^{std}$ . The timestep  $t$  then serves as a suitable insertion point for a blurry observation  $\tilde{y}_0^{std}$  with blur level  $std$ . To identify the optimal starting timestep  $t_{std}$  for each standard deviation, we use the following equation:

$$t_{std} = \underset{t}{\operatorname{argmin}} \quad (\log(\mathbf{X}_t) - \log(\tilde{\mathbf{Y}}_t^{std}) \leq tol), \quad (11)$$

where  $tol$  represents the maximum tolerance,  $\mathbf{X}_t$  and  $\tilde{\mathbf{Y}}_t^{std}$  denote the expected values of  $x_t$  and  $\tilde{y}_t^{std}$  in a training set.

Once we determine the corresponding starting timesteps for each standard deviation using Eq. (23), we store these pairs in the Dynamic Starting Step Lookup Table (DSST). Given an estimated  $\hat{std}^*$  via the SE network, the appropriate starting timestep can then be retrieved from the DSST.

## 4.3. Dynamic Guidance Scaling Adjuster

Region-specific adjustment on guidance scale  $s$  in Eq. (2) is crucial for diffusion sample refinement, as structured regions often require stronger diffusion (smaller  $s$ ), while smoother regions need weaker diffusion (larger  $s$ ). To address this, we propose the ‘‘Dynamic Guidance Scaling Adjuster (DGSA)’’, which adaptively adjusts  $s$  on a region-wise basis throughout the DM sampling process. By dynamically modulating the guidance scale, DGSA minimizes over-smoothing by preserving structural integrity in areas such as facial contours while enhancing realistic details by reducing the scale in fine-detail regions like hair and wrinkles. With DGSA incorporated, the proposed guidance formula is then modified as follows:

$$x_{t-1} = x'_{t-1} - A_t \times \nabla_{x_t} \|\hat{y} - k_t \otimes x_t^0\|^2, \quad t \leq t_{std} \quad (12)$$

$$A_t \equiv DGSA(\hat{y}, x_t^0, t). \quad (13)$$

In Eq. (13), DGSA is a CNN with three convolution layers, producing an output in the range  $[0, 1]$ . It takes as input the current measurement  $\hat{y}$ , the HQ prediction  $x_t^0$  based on  $x_t$ , and  $t$  to determine the local diffusion power needed at each timestep. The resulting output,  $A_t$ , is a region-wise guidance scaling map used to adjust the diffusion sampling.

The objective of training DGSA is to ensure that the HQ prediction  $x_{t-1}^0$ , based on  $x_{t-1}$  (as described in Eq. (3)), closely approximates the ground truth  $x_0$ . Here, the adjusted sample  $x_{t-1}$  is influenced by the DGSA network, as defined in Eq. (12). To achieve this, we randomly sample  $t$  and use the following loss function to train DGSA:

$$L_{DGSA} = \sum_i \gamma_i \mathbb{D}(SWT(x_{t-1}^0)_i, SWT(x_0)_i) + DIST(x_{t-1}^0, x_0), \quad (14)$$



Table 1. Comparisons with SOTA methods on CelebA-Test. The best and second-best performances are highlighted in **bold** and underline. For fairness, all methods are re-evaluated on the same test sets. Computational performance is measured on an RTX 3090 GPU.

Type	Method	Inference time (s)	MACs (G)	Params (M)	PSNR↑	SSIM↑	LPIPS↓	FID↓	IDA↓	LMD↓
GAN-based	GPEN	0.368	562.998	129.203	23.773	<u>0.659</u>	0.358	30.250	0.837	6.377
	GFP-GAN	0.123	45.228	76.207	22.841	0.620	0.355	23.860	0.822	4.793
Codebook-based	RestoreFormer	0.152	343.051	72.680	23.001	0.592	0.376	22.874	0.783	4.464
	CodeFormer	0.062	297.206	94.113	23.828	0.637	<b>0.319</b>	18.076	0.775	<u>3.509</u>
	DAEFR	0.288	455.605	152.151	21.640	0.589	0.345	15.983	0.870	3.917
DM-based	DiffBIR	11.280	1525.137	1716.700	24.127	0.647	0.357	19.194	<u>0.767</u>	3.535
	PGDiff	94.250	480.998	176.480	21.824	0.612	0.369	20.928	0.944	4.868
	DiffFace	6.120	272.678	175.430	23.949	<u>0.659</u>	0.355	<u>15.032</u>	0.867	3.781
	DR2	0.920	918.843	179.310	21.023	0.591	0.461	63.629	1.183	6.655
	3Diffusion	11.759	308.417	180.510	23.387	0.651	0.353	15.446	0.943	3.781
	DynFaceRestore	91.820	323.048	176.770	<b>24.349</b>	<b>0.664</b>	<u>0.332</u>	<b>14.780</b>	<b>0.748</b>	<b>3.419</b>

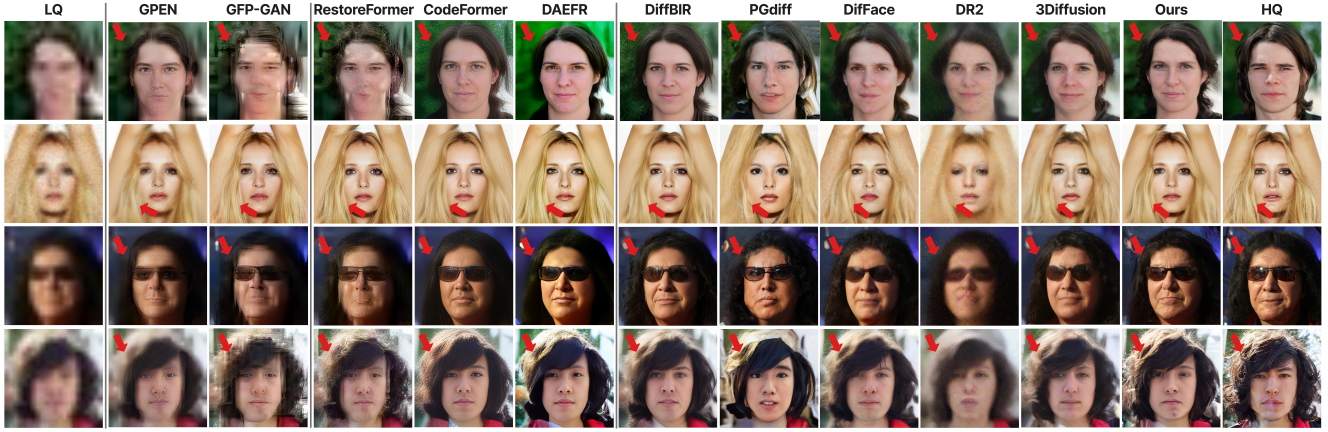


Figure 5. Qualitative results on CelebA-Test. Our method achieves high-fidelity reconstruction with visually accurate details, particularly in the mouth, hair, and skin texture. Please zoom in for the best view.

where  $\gamma_i$  are the weighted factors of the four subbands (LL, LH, HL, HH) decomposed by Stationary Wavelet Transformation (SWT) [15, 21], and  $DISTS$  [8, 21] is the perceptual loss. We would described in detail the full training procedure of our method in the Supplementary .

#### 4.4. Multiple Mapping and Guidance

Up to this point, we have employed only a single fidelity guidance,  $\hat{y}$ , and relied on the diffusion model (DM) to recover the missing high-frequency components (i.e., the difference between  $x$  and  $\hat{y}$ ) for restoration. However, while the DM effectively enhances image quality, it often sacrifices fidelity; conversely, the restoration model (RM) maintains fidelity but yields lower quality enhancement. To balance the strengths of DM and RM, we propose an optional add-on module that leverages multiple guidance sources. Specifically, once we obtain the estimated  $\hat{std}^*$  from SE, we generate three Gaussian-blurred guidance images  $\hat{y}^{i \in [1,2,3]}$  by varying  $std$  values. Formally,

$$\hat{y}^{i \in [1,2,3]} = k_y^{i \in [1,2,3]} \otimes RM(y), \quad (15)$$

Table 2. Comparisons to SOTA methods in real-world dataset (-Test). The best and second performances are highlighted with **bold** and underline.

Type	Method	LFW	WebPhoto	Wider
		FID↓	FID↓	FID↓
GAN-based	GPEN	51.942	80.705	46.359
	GFP-GAN	50.057	87.250	39.730
Codebook-based	RestoreFormer	48.412	<u>77.330</u>	49.839
	CodeFormer	52.350	83.193	38.798
	DAEFR	47.532	<b>75.453</b>	<u>36.720</u>
DM-based	DiffBIR	<u>43.446</u>	91.200	36.721
	PGDiff	44.942	84.163	40.380
	DiffFace	48.688	87.811	37.510
	DR2	70.979	117.090	76.550
	3Diffusion	46.888	83.335	37.130
	DynFaceRestore	<b>42.515</b>	95.317	<b>36.052</b>

where  $k_y^{i \in [1,2,3]}$  represents three Gaussian kernels with standard deviations  $std^*$ ,  $std^* - 1$ , and  $std^* - 2$ , respectively. These three guidance and corresponding kernels are then used in Eq. (12) to update the diffusion sample.

Since  $\hat{y}^1$  retains more trustworthy low-frequency structural information, while  $\hat{y}^2$  and  $\hat{y}^3$  provide more high-frequency



details but with lower confidence, we prioritize adjustments derived from  $\hat{y}^1$  by assigning it a higher weight, while assigning smaller weights to the guidance from  $\hat{y}^2$  and  $\hat{y}^3$ . Additionally, the standard deviation of  $k^{i \in [1,2,3]}$  are continuously adjusted throughout the diffusion process, as described in Eq. (7), which mitigates the impact of kernel mismatch and thereby enhances the fidelity of the final result. Nonetheless, one remaining issue is the selection of hyperparameters, including the number of guidance and the settings of *std* values, which can be explored in future work.

## 5. Experiments

### 5.1. Datasets and Metrics

**Training dataset.** Our framework is trained on the FFHQ dataset [17], which provides HQ facial images as the baseline. To simulate real-world degradation and generate LQ counterparts, we apply the following degradation pipeline:

$$y = \{JPG_{\delta}[(x \otimes k_{\sigma}) \downarrow_C + n_{\zeta}]\} \uparrow_C. \quad (16)$$

Here,  $\sigma$  represents the standard deviation of the blur kernel, uniformly sampled from [0.1, 15]. The scale factor  $C$ , used for both downsampling and upsampling, is uniformly sampled from [0.8, 32]. The noise level  $\zeta$  is also uniformly sampled from [0, 20], and  $\delta$  denotes the JPEG compression quality factor, uniformly sampled from [30, 100]. We use the same hyperparameters settings as [28].

**Testing datasets** We evaluate our method on one synthetic dataset (CelebA) and three real-world datasets (LFW, WebPhoto, and Wider). The CelebA-Test dataset comprises 3,000 LQ facial images synthesized from the CelebA-HQ [16] validation set using the degradation pipeline outlined in Eq. (18). For real-world testing, LFW-Test [14], consists of 1,711 slightly degraded images, each representing a unique individual from the LFW dataset; WebPhoto-Test [22] comprises 407 internet-sourced images, including heavily degraded old photos; and Wider-Test [43] features 970 severely degraded images from the Wider dataset [39]. These datasets, encompassing varying levels of degradation, enable a comprehensive evaluation of our method’s robustness and effectiveness in real-world scenarios.

**Evaluation metrics** PSNR and SSIM are used for the synthetic dataset to assess fidelity, while LPIPS [42] measures perceptual quality. IDA evaluates identity consistency based on embeddings from ArcFace [6], and LMD [33] assesses facial alignment and expression accuracy. Finally, FID [12] is employed to evaluate perceptual quality. For the synthetic testing case, the CelebA-HQ dataset is used as the reference set; for real-world testing, the FFHQ dataset forms the reference set.

To ensure a fair comparison, we utilized the same pre-trained diffusion model as DiffFace [41] and PGDiff [38].

Due to space limitations, comprehensive implementation details, hyperparameter configurations, training procedures, and additional results are provided in the Supplementary.

### 5.2. Comparisons to SOTA methods

We conduct comprehensive quantitative and qualitative comparisons of our proposed DynFaceRestore with the following state-of-the-art BFR methods: *GAN – based* (GPEN [40], GFPGAN [22]), *Codebook – based* (RestoreFormer [36], CodeFormer [43], DAEFR [33]) and *DiffusionModel(DM) – based* (DiffBIR [26], PGDiff [38], DiffFace [41], DR2 [37] and 3Diffusion [27]).

**Comparison on Synthetic Dataset.** Tab. 1 presents the quantitative results on the CelebA-Test dataset, demonstrating our method outperforms others in PSNR, SSIM, FID, IDA, and LMD metrics, while ranking second in LPIPS. These results highlight the method’s ability to balance fidelity and perceptual quality well.

Qualitative results in Fig. 5 further highlight the advantages of our method. GAN-based approaches often introduce artifacts, while codebook-based methods generate high-quality details but still suffer from fidelity issues. Similarly, diffusion-based methods exhibit deviations from the ground truth. In contrast, our method consistently achieves high-fidelity reconstructions, preserving critical features such as the mouth, hair, and skin texture while maintaining image quality across varying degradation levels. This demonstrates its ability to produce visually accurate results.

**Comparison on Real-world Datasets.** In Tab. 2, we provide quantitative results across three real-world datasets, showing that our method surpasses competing approaches by achieving the best FID scores on the LFW-Test and the Wider-Test. For the WebPhoto-Test, it is worth noting that the FID score may not accurately reflect the discrepancy from the actual data distribution, given the dataset’s smaller sample size of 407 images, as also noted in prior works such as DiffFace [41] and WaveFace [28].

Fig. 6 showcases qualitative results on these real-world datasets. GAN-based methods often produce artifacts that compromise the quality crucial for BFR. While Codebook-based and DM-based methods demonstrate improvements in realism, our approach achieves higher perceptual quality across varying degradation levels. These observations show the ability to produce high-quality details of DynFaceRestore.

### 5.3. Ablation Study

We evaluate various model aspects depending on different settings ( $A, B, C, D, E, F$ ) as shown in Tab. 3 and Fig. 7, along with a *Baseline* comparison leveraged diffusion model [7] trained on the FFHQ [17].

**Effect of DBLM.** Compared to the *Baseline*, setting **A** achieves remarkable improvements across all metrics by re-

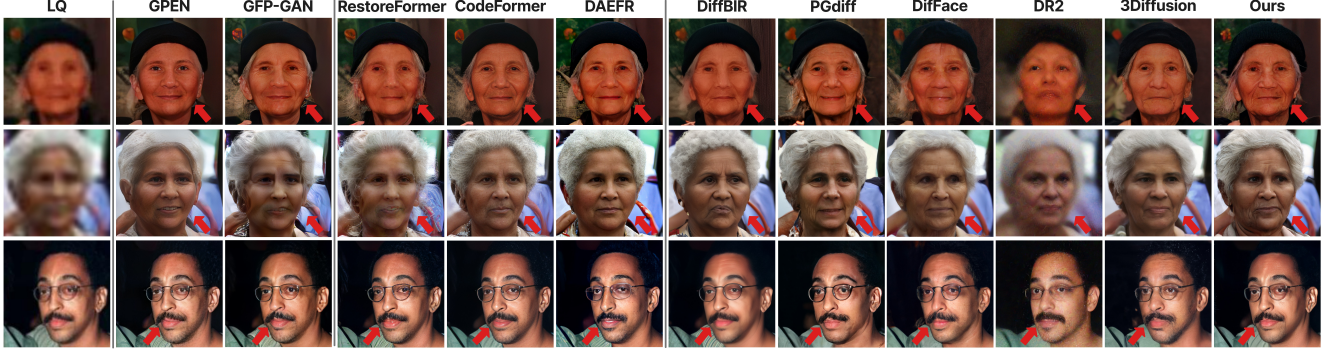


Figure 6. Qualitative results from three real-world datasets demonstrate that our restoration method produces more natural features (e.g., eyes) and realistic details (e.g., hair) compared to other approaches, with improved fidelity. Please zoom in for the best view.

Table 3. Ablation study of our framework on CelebA-Test. The best performance is highlighted with **bold**.

Setting	<i>DBLM</i>	<i>Multiple Guidance</i>	<i>DSST</i>	<i>DGSA</i>	PSNR $\uparrow$	SSIM $\uparrow$	FID $\downarrow$	IDA $\downarrow$	Range of sampling steps
Baseline (DM)					11.129	0.382	55.777	1.461	1000
A	✓				24.992	0.690	18.303	0.725	1000
B	✓	✓			25.094	0.694	19.823	0.725	1000
C	✓	✓	✓		<b>25.107</b>	<b>0.695</b>	19.786	<b>0.724</b>	[690, 925]
D	✓	✓		✓	24.340	0.664	15.007	0.750	1000
E	✓		✓	✓	24.327	0.666	<b>14.689</b>	0.755	[690, 925]
F	✓	✓	✓	✓	24.349	0.664	14.780	0.748	[690, 925]

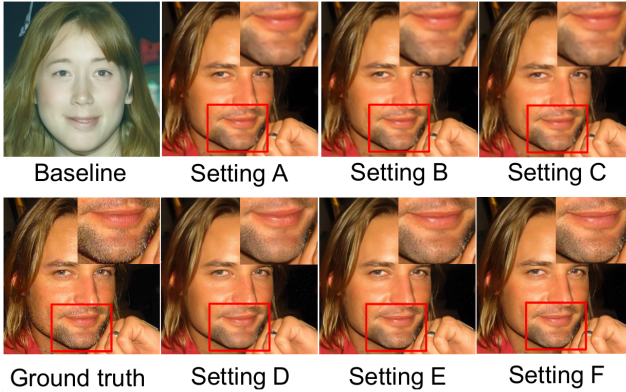


Figure 7. Ablation results for each component in DynFaceRestore are shown, using the experimental settings in Tab. 3 for visual comparison. With the addition of DBLM, DSST, DGSA, and multiple guidance, DynFaceRestore well balances fidelity and quality.

framing the BFR task as Gaussian deblurring and incorporating DM guidance. As shown in Fig. 7, the mouth and beard regions in setting **A** are closer to Ground Truth.

**Effect of Multiple Guidance.** Setting **B** and **F** further enhance fidelity over **A** and **E**, respectively, improving both PSNR and IDA metrics by adaptively incorporating multiple guidance sources. Specifically, three Gaussian-blurred images are applied to guide the diffusion sampling process in this experiment.

**Effect of DSST.** Compared to setting **B**, integrating the DSST table in setting **C** improves both PSNR and FID,

while also shortening the sampling process, as reflected in the reduced range of sampling steps. This improvement is achieved by identifying the optimal starting step, effectively avoiding under- or over-diffusion.

**Effect of DGSA.** Setting **D**, **E**, **F** achieves a notable improvement in the perceptual quality (FID score) compared to settings **A**, **B**, **C**, as illustrated in Fig. 7 and Tab. 3. This demonstrates the effectiveness of the region-wise guidance scale. Visual analysis of the scaling map is provided in the Supplementary to explain the DGSA’s behavior.

Our approach provides dynamic control, ranging from enhancing fidelity restoration (setting **C**) to effectively improving image quality, achieving the best FID score (setting **E**). This highlights the flexibility of our model, allowing us to balance perceptual quality and fidelity by managing guidance resources (setting **F**).

## 6. Conclusion

We propose DynFaceRestore for Blind Face Restoration (BFR). By utilizing Dynamic Blur-Level Mapping, we simplify the task by mapping unknown degraded input to a corresponding Gaussian blurred image, effectively reframing BFR as a Gaussian deblurring problem. Combined with optimal starting steps and region-wise scale adjustments, our method delivers superior performance. Experimental results demonstrate that DynFaceRestore outperforms existing methods while striking a balance between fidelity and perceptual quality. Additional experiments, comparisons, and analyses are provided in the Supplementary.

# DynFaceRestore: Balancing Fidelity and Quality in Diffusion-Guided Blind Face Restoration with Dynamic Blur-Level Mapping and Guidance

## Supplementary Material

### A. Implementation Details

#### A.1. Dynamic Blur-Level Mapping

**Architecture:** With the objective of transforming the degraded input  $y$  into a Gaussian-blurred counterpart  $\hat{y}$ , the proposed Dynamic Blur-Level Mapping (DBLM) is composed of two primary modules: the Standard Estimation ( $SE$ ) module and the Restoration Model ( $RM$ ). Specifically, the  $SE$  predicts the Gaussian blur standard deviation  $\hat{std}^*$  corresponding to  $y$ , while the  $RM$  refines  $y$  into the high-quality (HQ) distribution. The final Gaussian-blurred output, as described in Eq. (8) of the main paper, is rewritten as follows:

$$\hat{y} = k^{\hat{std}^*} \otimes RM(y), \quad (17)$$

where  $RM$  represents any SOTA pre-trained restoration model capable of mapping degraded inputs directly to high-quality (HQ) outputs. In our experiments, we adopt SwinIR [25] architecture, which has been well-trained in DiffFace [41].  $k^{\hat{std}^*}$  denotes as Gaussian blur kernel defined by  $\hat{std}^*$  estimated by  $SE$  module.

As shown in Fig. 8, the  $SE$  comprises a Transfer Model ( $TM$ ) and a Standard Deviation Estimator ( $SDE$ ). The  $TM$ , built on the SwinIR architecture [25], converts the degraded input  $y$  into an intermediate Gaussian-blurred image  $\hat{y}'$ . Subsequently, the  $SDE$  processes this intermediate image to estimate the corresponding Gaussian blur level  $\hat{std}^*$ . The detailed architecture of the  $SDE$  is provided in Tab. 4.

**Data Preparation for Training  $SE$ :** To train the  $SE$  module and implement the concept of DBLM, we first prepare the training labels. Specifically, for synthesized low-quality (LQ) facial images, we collect pairs of ground truth labels: (1) kernel standard deviations  $std^*$  to supervise the  $SDE$  and (2) Gaussian-blurred images  $\tilde{x}$ , generated by degrading the high-quality (HQ) image  $x$  using  $k^{std^*}$ , to supervise the  $TM$ . The synthesized low-quality (LQ) facial images  $y$  are created using the degradation pipeline described below:

$$y = \{JPEGS_\delta[(x \otimes k_\sigma) \downarrow_C + n_\zeta]\} \uparrow_C. \quad (18)$$

Here, we use the same hyperparameter settings as [28] for synthesizing low-quality (LQ) facial images. Additionally, the kernel standard deviation label  $std^*$  is determined by using Eq. (19), and the corresponding Gaussian-blurred ground truth is generated using  $\tilde{x} \equiv k_y^{std^*} \otimes x$ .

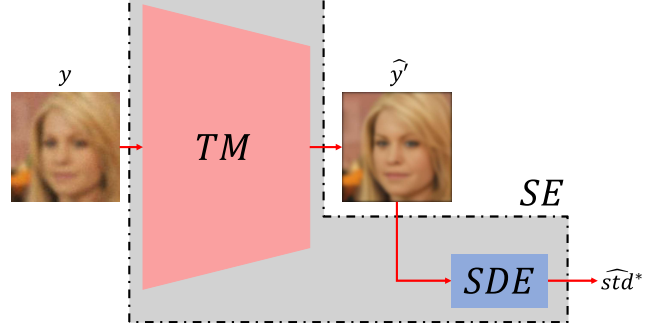


Figure 8. The  $SE$  consists of  $TM$  and a  $SDE$ , predicting the Gaussian blur level corresponding to the degraded input based on intermediate Gaussian blur image  $\hat{y}'$ .

$$\begin{aligned} std^* &\equiv \arg \min_{std \in [std_{min}, std_{max}]} (std), \\ \text{s.t. } &\|k^{std} \otimes RM(y) - k^{std} \otimes x\|^1 < \xi. \end{aligned} \quad (19)$$

Here,  $\xi$  represents the error tolerance,  $x$  denotes the high-quality (HQ) ground truth, and  $\otimes$  signifies the convolution operation. The search space for the standard deviation range,  $[std_{min}, std_{max}]$ , is defined between 0.1 and 15.0 with an interval of 0.1. To solve the optimization problem in Eq. (19), we employ a brute-force method.

**Training procedure of  $SE$ :** The training procedure of  $SE$  begins with  $SDE$  within the  $SE$ . Here, Gaussian-blurred images are generated by Eq. (20) and used to train the  $SDE$  by  $L_{SDE}$  defined in Eq. (21).

$$\tilde{y} = k^{\tilde{std}} \otimes x. \quad (20)$$

$L_{SDE}$  denotes the loss function that aligns the  $SDE$ 's predictions with the actual blur levels  $\tilde{std}$ . After completing this training phase, the  $SDE$  reliably estimates the Gaussian kernel for any Gaussian-blurred image, forming a robust foundation for effective blur-level prediction in the subsequent stages of the DBLM framework.

$$L_{SDE} = \mathbb{D}(SDE(\tilde{y}), \tilde{std}). \quad (21)$$

Subsequently, we train the whole  $SE$  in an end-to-end manner, where the  $SDE$  and  $TM$  modules in the  $SE$  are trained using the following loss:

$$L_{SE} = \mathbb{D}(\hat{std}^*, std^*) + \gamma_{std} \mathbb{D}(\hat{y}', \tilde{x}), \quad (22)$$



Table 4. Architecture of  $SDE$ .

architecture	channels
Conv2d: kernel size: $3 \times 3$ ; stride: 1	$3 \rightarrow 64$
BatchNormalize2d	64
LeakyReLU	-
Conv2d: kernel size: $3 \times 3$ ; stride: 1	$64 \rightarrow 64$
BatchNormalize2d	64
LeakyReLU	-
Conv2d: kernel size: $3 \times 3$ ; stride: 2	$64 \rightarrow 128$
BatchNormalize2d	128
LeakyReLU	-
Conv2d: kernel size: $3 \times 3$ ; stride: 1	$128 \rightarrow 128$
BatchNormalize2d	128
LeakyReLU	-
Conv2d: kernel size: $3 \times 3$ ; stride: 2	$128 \rightarrow 256$
BatchNormalize2d	256
LeakyReLU	-
Conv2d: kernel size: $3 \times 3$ ; stride: 1	$256 \rightarrow 256$
BatchNormalize2d	64
LeakyReLU	-
AvgPool2d	-
Linear	$256 \rightarrow 256$
LeakyReLU	-
Linear	$256 \rightarrow 256$
Linear	$256 \rightarrow 1$

where  $\mathbb{D}$  is the L1 distance,  $\gamma_{std}$  is a weighting factor for balancing,  $\hat{std}^*$  is the output of  $SDE$ ,  $\hat{y}'$  is the output of  $TM$ , and  $\tilde{x} \equiv k_y^{std*} \otimes x$ . This allows the  $SE$  to accurately predict the Gaussian blur level corresponding to any degraded input  $y$ .

Finally, as described in the main paper, the  $SE$  and  $RM$  are integrated to form the proposed DBLM, transforming the unknown degraded input  $y$  into its corresponding Gaussian-blurred version  $\hat{y}$ . This transformation simplifies the Blind Face Restoration task into a Gaussian deblurring problem.

## A.2. Dynamic Starting Step Look-up Table

As mentioned in Sec.4.2 in our main paper, the optimal starting timestep  $t_{std}$  for each standard deviation is defined as follows:

$$t_{std} = \underset{t}{\operatorname{argmin}} \quad (\log(\mathbf{X}_t) - \log(\tilde{\mathbf{Y}}_t^{std}) \leq tol), \quad (23)$$

where  $tol$  represents the maximum tolerance,  $\mathbf{X}_t$  and  $\tilde{\mathbf{Y}}_t^{std}$  denote the expected values of  $x_t$  and  $\tilde{y}_t^{std}$  in a training set. We set  $tol$  to  $1 \times 10^{-3}$  to construct the Dynamic Starting Step Look-up Table (DSST), which pairs each standard deviation  $std$  with its corresponding starting step  $t_{std}$ . Given the Gaussian-blur image  $\hat{y}$ , the estimated standard deviation  $\hat{std}^*$  from  $SE$  is equalized and serves as a key to retrieve the corresponding starting step from the DSST.

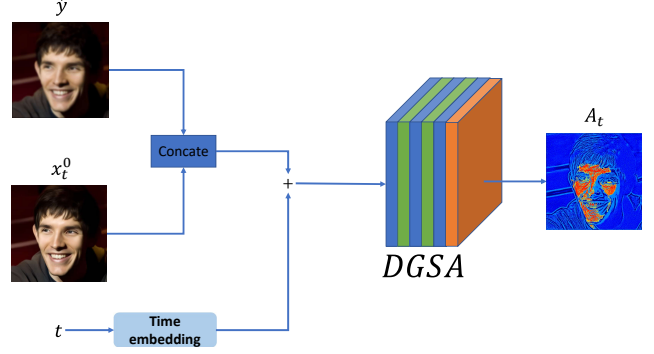


Figure 9. The inference flow of the DGSA is as follows: the measurement  $\hat{y}$  and the high-quality prediction  $x_t^0$  from  $x_t$  are first concatenated to form a combined input. This concatenated input is then integrated with the current timestep  $t$ , which is processed through the time embedding module of the diffusion model. The resulting features are input into DGSA, generating a region-specific guidance scale map that dynamically adjusts the guidance scale at each timestep to balance fidelity and detail preservation.

Table 5. Network architecture of DGSA.

architecture	channels
Conv2d: kernel size: $3 \times 3$	$6 \rightarrow 64$
ELU	-
Conv2d: kernel size: $3 \times 3$	$64 \rightarrow 64$
ELU	-
Conv2d: kernel size: $3 \times 3$	$64 \rightarrow 3$
ReLU-1	-

## A.3. Dynamic Guidance Scale Adjuster

**Network Architecture:** The architecture of the Dynamic Guidance Scale Adjuster (DGSA) is outlined in Tab. 5. DGSA consists of three convolutional layers, with ELU activation functions applied after the first two layers. The final layer uses the ReLU-1 activation function to constrain the output within the range of 0 to 1. At timestep  $t$ , the inputs to DGSA include the degraded measurement  $\hat{y}$ , the high-quality (HQ) prediction  $x_t^0$  derived from  $x_t$ , and the current timestep  $t$ .

In the implementation of DGSA, as illustrated in Fig. 9,  $\hat{y}$  and  $x_t^0$  are concatenated before being input into the DGSA. This design ensures that the model effectively captures low-frequency information from both inputs to preserve fidelity. The timestep  $t$  is then embedded and combined with the concatenated features to determine the localized diffusion power required at each region and timestep. The output of DGSA is a pixel-wise guidance scale map with values ranging from 0 to 1, matching the image dimensions. Higher values indicate stronger guidance influence to preserve fidelity, while lower values relax the guidance to utilize the DM’s realistic facial generation capabilities. This behavior is visualized in Fig. 12.



---

**Algorithm 2** DGSA training
 

---

**Require:**  $y$ : Unknown degraded LQ input;  $iter_{total}$ : Total training iterations;  $\gamma_i$ : Weight factor of SWT four subbands;

- 1:  $iter = 0$ ;
- 2: **while**  $iter < iter_{total}$  **do**
- 3:  $\hat{y}, std^* = DBLM(y), SE(y)$ ;
- 4:  $t_{start} = DSST(std^*)$ ;
- 5:  $t \sim Uniform(0, t_{start})$ ;
- 6:  $x_t = \sqrt{\alpha_t}x_0 + \sqrt{1 - \alpha_t}\epsilon, \epsilon \sim N(0, 1)$ ;
- 7:  $x_t^0 = \frac{1}{\sqrt{\alpha_t}}x_t - \sqrt{\frac{1 - \alpha_t}{\alpha_t}}\epsilon_\theta$ ;
- 8: compute Gaussian blur kernel  $k$  using  $std^*$ ;
- 9:  $x'_{t-1} = \frac{1}{\sqrt{\alpha_t}}(x_t - \frac{\beta_t}{\sqrt{1 - \alpha_t}}\epsilon_\theta) + \sigma_t\epsilon, \epsilon \sim N(0, 1)$ ;
- 10:  $A_t = DGSA(\hat{y}, x_t^0, t)$
- 11:  $x_{t-1} = x'_{t-1} - A_t \times \nabla_{x_t} \|\hat{y} - k_t \otimes x_t^0\|^2$ ;
- 12:  $x_{t-1}^0 = \frac{1}{\sqrt{\alpha_{t-1}}}x_{t-1} - \sqrt{\frac{1 - \alpha_{t-1}}{\alpha_{t-1}}}\epsilon_\theta$ ;
- 13:  $L_{DGSE} = \sum_i \gamma_i \mathbb{D}(SWT(x_{t-1}^0)_i, SWT(x_0)_i)$
- 14:  $\quad + \quad DIST(S(x_{t-1}^0, x_0))$ ;
- 15: update DGSA using  $L_{DGSE}$ ;
- 16:  $iter = iter + 1$ ;
- 17: **end while**

---

**Training procedure:** The DGSA training process is divided into two stages for optimal performance. Initially, DGSA is trained using actual Gaussian blurry images  $\tilde{y}$  as the measurement inputs, generated based on Eq. (20). That is, we replace the output of DBLM  $\hat{y}$  with  $\tilde{y}$  in this stage. This stage consists of 20,000 iterations, allowing DGSA to learn robust guidance scale mappings for well-defined blurry images as its measurement input. In the second stage, DGSA undergoes fine-tuning with its original input,  $\hat{y}$ , representing the measurement predicted by our DBLM. This fine-tuning phase, spanning 7,000 iterations, further refines DGSA’s ability to adapt to real-world degraded inputs. During training, the DBLM module is kept frozen, and the DSST is pre-established.

We train DGSA at each randomly sampled timestep using the following loss function:

$$L_{DGSA} = \sum_i \gamma_i \mathbb{D}(SWT(x_{t-1}^0)_i, SWT(x_0)_i) + DIST(S(x_{t-1}^0, x_0)), \quad (24)$$

where  $\gamma_i$  are the weighted factors of the four subbands (LL, LH, HL, HH) decomposed by Stationary Wavelet Transformation (SWT) [15, 21],  $x_0$  is the learning target, and  $x_{t-1}^0$  is the HQ prediction based on  $x_{t-1}$  at timestep  $t - 1$ . Here,  $\mathbb{D}$  and  $DIST$  [8, 21] are the L1 reconstruction loss and the perceptual loss, respectively.

The L1 reconstruction loss is applied across four subbands obtained via Stationary Wavelet Transform (SWT), with weighted factors  $\gamma_i$  for LL, LH, HL, and HH set to 0.00, 0.01, 0.01, and 0.05, respectively. These weights prioritize high-frequency details, ensuring that the details of

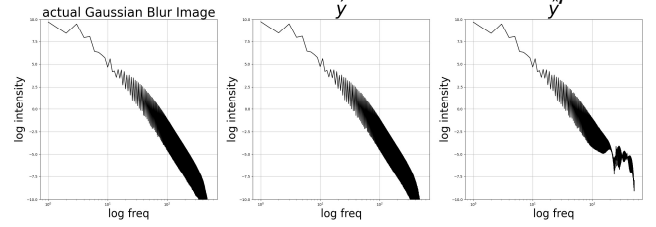


Figure 10. The frequency responses of actual Gaussian blurry images,  $\hat{y}$ , and  $\hat{y}'$ . Here,  $\hat{y}'$ , the output of  $TM$  (refer to Fig. 8), exhibits significant differences in the high-frequency components compared to actual Gaussian-blurred images. In contrast,  $\hat{y}$ , estimated using Eq. (17), closely matches the frequency response of the actual Gaussian-blurred image.

the samples adjusted by guidance remain consistent with the ground truth. Furthermore, we utilize DISTs to maintain the perceptual quality of the output. The complete training procedure is detailed in Algorithm 2.

#### A.4. Inference

Our DynFaceRestore framework is designed to be easily extendable, allowing for the use of multiple guidance sources. This flexibility enables a balance between perceptual quality and fidelity. In all our experiments, we utilize guidance from three blurred images, as outlined in Algorithm 3, with the weights  $\lambda^{i \in [1, 2, 3]}$  are set to 0.7, 0.2, and 0.1, respectively. Further experimental analysis and discussions regarding the multiple guidance setup are provided in Appendix B.3.

## B. Extra Experiments and Ablation Studies

### B.1. Kernel Mismatch

**The difference between  $\hat{y}'$  and  $\hat{y}$ :** The analysis in Fig. 10 provides a detailed comparison between  $\hat{y}'$  and  $\hat{y}$ , offering a strong rationale for designing the DBLM output as  $\hat{y}$  rather than directly using the output of  $TM$ ,  $\hat{y}'$ . By transforming  $\hat{y}'$  and  $\hat{y}$  into the frequency domain, a significant disparity in high-frequency intensity emerges when comparing  $\hat{y}'$  to actual Gaussian-blurred images.

In contrast, explicitly convolving the output of  $RM(y)$  with a Gaussian kernel to produce  $\hat{y}$  yields high-frequency intensity closely aligned with that of actual Gaussian-blurred images. This alignment suggests that the high-frequency discrepancy in  $\hat{y}'$  is a crucial contributor to kernel mismatch, adversely affecting restoration fidelity. Furthermore, the quantitative results in Tab. 6 confirm these findings, showing that using  $\hat{y}$  as diffusion guidance in DBLM achieves superior fidelity over  $\hat{y}'$ , further validating the effectiveness of explicitly constructing  $\hat{y}$ .

**Refinement of the Standard Deviation:** In Fig. 11, experimental evidence highlights the critical role of kernel re-

---

**Algorithm 3** Inference - Multiple Guidance
 

---

**Require:**  $y$ : Unknown degraded LQ input;  $\lambda^{i \in [1,2,3]}$ : weights of each guidance;

**Ensure:**  $x_0$ : HQ sampled image;

```

1:  $\hat{y}, \hat{std}^* = DBLM(y), SE(y)$ ;
2:  $\hat{std}^{*i \in [1,2,3]} = [\hat{std}^*, \hat{std}^* - 1, \hat{std}^* - 2]$ 
3: compute Gaussian blur kernel  $k^{i \in [1,2,3]}$  using  $\hat{std}^{*i \in [1,2,3]}$ ;
4:  $\hat{y}^{i \in [1,2,3]} = [\hat{y}, k^2 \otimes RM(y), k^3 \otimes RM(y)]$ 
5:  $t_{start}^{i \in [1,2,3]} = DSST(\hat{std}^{*i \in [1,2,3]})$ ;
6:  $\hat{std}_{t_{start}}^{i \in [1,2,3]} = \hat{std}^{*i \in [1,2,3]}$ ;
7:  $x_{t_{start}} = \sqrt{\bar{\alpha}_{t_{start}}^1} \hat{y}^1 + \sqrt{1 - \bar{\alpha}_{t_{start}}^1} \epsilon, \epsilon \sim N(0, 1)$ ;
8: for  $t = t_{start}^1 \cdots 1$  do
9:    $x_t^0 = \frac{1}{\sqrt{\bar{\alpha}_t}} x_t - \sqrt{\frac{1 - \bar{\alpha}_t}{\bar{\alpha}_t}} \epsilon_\theta$ ;
10:   $x_{t-1} = \frac{1}{\sqrt{\bar{\alpha}_t}} (x_t - \frac{\beta_t}{\sqrt{1 - \bar{\alpha}_t}} \epsilon_\theta) + \sigma_t \epsilon, \epsilon \sim N(0, 1)$ ;
11:  compute Gaussian blur kernel  $k_t^{i \in [1,2,3]}$  using  $\hat{std}_t^{i \in [1,2,3]}$ ;
12:   $A_t = DGSA(\hat{y}^1, x_t^0, t)$ ;
13:  if  $t \in [t_{start}^1, t_{start}^2]$  then
14:     $x_{t-1} = x'_{t-1} - A_t \times \nabla_{x_t} \|\hat{y}^1 - k_t^1 \otimes x_t^0\|^2$ ;
15:     $\hat{std}_{t-1}^1 = \hat{std}_t^1 - \sqrt{\bar{\alpha}_t} \times \nabla_{k_t^1} \|\hat{y}^1 - k_t^1 \otimes x_t^0\|^2$ ;
16:  end if
17:  if  $t \in [t_{start}^2, t_{start}^3]$  then
18:     $x_{t-1} = x'_{t-1} - A_t \times \nabla_{x_t} \sum_{i=1}^2 (\frac{\lambda^i}{\lambda^1 + \lambda^2}) \|\hat{y}^i - k_t^i \otimes x_t^0\|^2$ ;
19:     $\hat{std}_{t-1}^{i \in [1,2]} = \hat{std}_t^{i \in [1,2]} - \sqrt{\bar{\alpha}_t} \times \nabla_{k_t^{i \in [1,2]}} (\frac{\lambda^i}{\lambda^1 + \lambda^2}) \|\hat{y}^{i \in [1,2]} - k_t^{i \in [1,2]} \otimes x_t^0\|^2$ ;
20:  end if
21:  if  $t \in [t_{start}^3, 0]$  then
22:     $x_{t-1} = x'_{t-1} - A_t \times \nabla_{x_t} \sum_{i=1}^3 (\frac{\lambda^i}{\lambda^1 + \lambda^2 + \lambda^3}) \|\hat{y}^i - k_t^i \otimes x_t^0\|^2$ ;
23:     $\hat{std}_{t-1}^{i \in [1,2,3]} = \hat{std}_t^{i \in [1,2,3]} - \sqrt{\bar{\alpha}_t} \times \nabla_{k_t^{i \in [1,2,3]}} (\frac{\lambda^i}{\lambda^1 + \lambda^2 + \lambda^3}) \|\hat{y}^{i \in [1,2,3]} - k_t^{i \in [1,2,3]} \otimes x_t^0\|^2$ ;
24:  end if
25: end for
26: return  $x_0$ 

```

---

Table 6. Ablation study on different output types of DBLM in the CelebA-Test dataset. Here,  $\hat{y}'$  and  $\hat{y}$  represent different approximations of the Gaussian-blurred image  $\tilde{x}$ . The results clearly show that  $\hat{y}$  provides a closer approximation of  $\tilde{x}$ , resulting in improved fidelity.

Gaussian Blur image	PSNR $\uparrow$	SSIM $\uparrow$	LPIPS $\downarrow$	FID $\downarrow$	IDA $\downarrow$	LMD $\downarrow$
$\hat{y}'$	24.261	0.661	0.332	<b>14.185</b>	0.756	3.428
$\hat{y}$	<b>24.349</b>	<b>0.664</b>	0.332	14.780	<b>0.748</b>	<b>3.419</b>

finement at each step in mitigating kernel mismatch during the sampling process. Using an actual Gaussian blur measurement with a kernel of  $std = 3.0$  as the guidance, the experiment in Fig. 11 evaluates outcomes without employing DBLM, DSST, or DGSA to focus solely on analyzing the kernel refinement function. When the kernel std is not refined and fixed to the wrong standard deviation at each

step, a substantial deviation between the final sampled results and the ground truth is evident, even with guidance applied. Notably, the results closely align with the ground truth only when the kernel std is accurately set to 3.0, as further validated by the ‘‘PSNR over std’’ analysis shown in Fig. 11.

In contrast, with kernel std refinement applied at each step, the sampled results exhibit remarkable fidelity to the ground truth, even when the initial kernel std estimation deviates from the actual value. This outcome underscores the robustness of the kernel refinement strategy in addressing inaccuracies in initial kernel estimation, effectively bridging the gap caused by kernel mismatch. These findings validate the necessity of dynamic kernel std adjustments to achieve high-quality restoration.

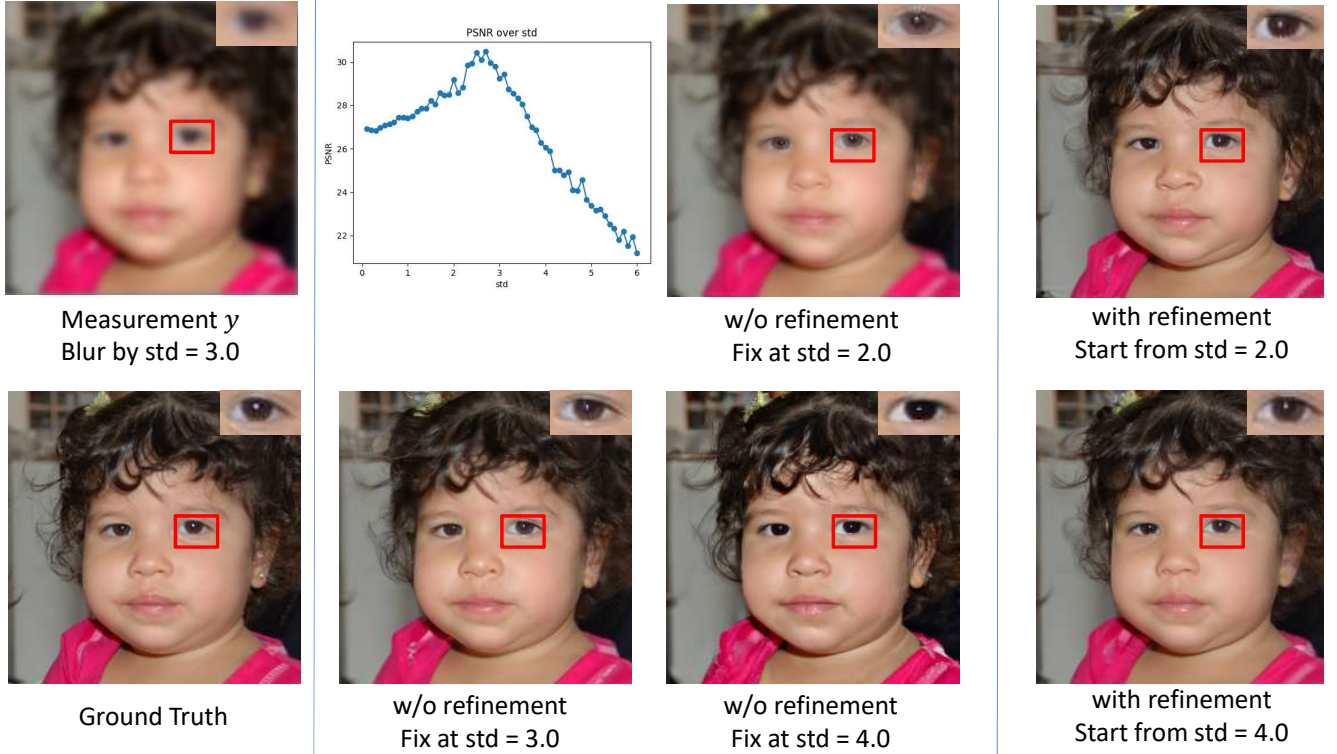


Figure 11. Comparison of results with and without kernel refinement is conducted using an actual Gaussian-blurred image with a kernel standard deviation (std) of 3.0 as the input measurement for guidance. During the diffusion sampling process, applying guidance adjustment without kernel refinement—e.g., fixing the kernel std to 2.0 or 4.0—leads to significant deviations from the ground truth due to kernel mismatch. When the fixed std is set to 2.0, the mismatch limits the diffusion model’s ability to add details, resulting in overly blurry outputs that rely too heavily on the measurement. Conversely, with a fixed std of 4.0, the diffusion model overly enhances the image, introducing hallucinated artifacts. In contrast, incorporating kernel refinement alongside guidance adjustment enables the sampling process to correct initial inaccuracies in kernel prediction. Even when starting with an imperfect kernel std, such as 2.0 or 4.0, the refined approach ensures that the final outputs align much more closely with the ground truth. This demonstrates the robustness of the refinement strategy in mitigating kernel mismatch issues.

## B.2. Visualize of DGSA

The output of DGSA is visualized in Fig. 12 to highlight its effectiveness. In each diffusion timestep, DGSA dynamically adjusts the guidance scale region-wise. The guidance scale gradually decreases for detail-rich areas such as hair and wrinkles, enabling these regions to harness more of the pre-trained DM’s high-quality image prior to sampling, resulting in realistic and refined facial details. Conversely, the guidance scale remains elevated for structural regions, such as the eyes and mouth, to preserve their geometric integrity and ensure the reconstructed image aligns closely with the ground truth. This adaptive balance between fidelity and detail generation leads to high realism outputs while maintaining structural consistency.

## B.3. Multiple Guidance

In this section, we evaluate the impact of varying the number of guidance sources. To ensure accurate assessment,

DGSA is excluded to eliminate any potential external influences in this experiment. Each guidance source corresponds to a specific standard deviation, which changes following a defined pattern. For example, with  $n$  guidance sources, we have  $\hat{y}^{i \in [1, 2, \dots, n]}$  corresponding to the standard deviations  $\hat{std}^*, \hat{std}^* - 1, \dots, \hat{std}^* - (n - 1)$  and the weights  $\lambda^{i \in [1, 2, \dots, n]}$ .

Since  $\hat{y}^1$  with  $\hat{std}^*$  retains more reliable low-frequency structural information,  $\lambda^1$  is assigned a higher weight. In contrast, smaller standard deviations values  $\hat{y}^{i \in [2, 3, 4]}$  provide higher-frequency details with reduced confidence, and thus,  $\lambda^{i \in [2, 3, 4]}$  are assigned lower weights, as outlined by  $\lambda^i$  in Tab. 7.

As shown in Tab. 7, increasing the number of guidance sources amplifies the influence of the restoration model (RM), resulting in improved fidelity and higher scores in PSNR. However, perceptual quality (FID) is optimized when using a single guidance source, which allows more

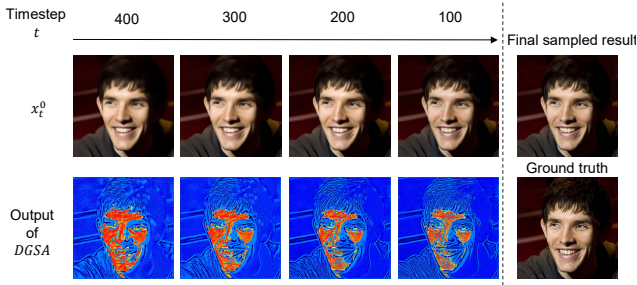


Figure 12. Visualization of DGSA at various timesteps during the sampling process. Here,  $x_t^0$  is the HQ prediction of  $x_t$  at timestep  $t$ . DGSA generates guidance maps, where blue regions indicate less guidance and rely more on the diffusion model (DM) to add details, while red regions signify stronger guidance with less reliance on the DM. As  $t$  decreases, areas requiring the DM’s HQ prior, such as hair, display a lower guidance scale to enhance detail. Conversely, facial regions maintain a higher guidance scale to ensure fidelity preservation.

Table 7. Ablations of the different numbers of guidance in CelebA-Test dataset. # denotes the numbers of guidance and  $\lambda^i$  are the weights of each guidance. The best performance is highlighted with **bold**.

#	$\lambda^i$	PSNR $\uparrow$	IDA $\downarrow$	FID $\downarrow$
1	[1.0]	25.014	0.7242	<b>18.452</b>
2	[0.8, 0.2]	25.049	0.7238	18.98
3	[0.7, 0.2, 0.1]	25.107	<b>0.7236</b>	19.786
4	[0.7, 0.1, 0.1, 0.1]	<b>25.185</b>	0.7242	20.947

reliance on the diffusion model. This demonstrates the flexibility of our framework, enabling users to tune the desired output by controlling the number of guidance sources. Consequently, our framework effectively achieves a balance between perceptual quality and fidelity.

#### B.4. Different Starting Steps

By setting up the output of DBLM as a Gaussian-blurred image based on the input degradation severity, we can leverage this property to identify the optimal timestep ( $t^*$ ), as outlined in Sec. 4.2 using “Dynamic Starting Step Lookup Table”. Note that  $t^*$  is automatically determined for different datasets. To demonstrate the effectiveness of our approach, we conduct experiments with different starting timesteps, as shown in Tab. 8. Larger timesteps ( $> t^*$ ) result in a loss of information from the guidance observation, leading to reduced fidelity. Conversely, smaller timesteps ( $< t^*$ ) provide insufficient iterations to recover fine details, thereby diminishing the quality of the reconstruction.

#### B.5. Different SOTA Restoration Model

We evaluate the impact of different Restoration Models (RMs) on overall performance by replacing our pre-

Table 8. Ablation study of same blurred image with different starting steps in CelebA-Test. Top performances in **bold** and underline.

Steps	PSNR $\uparrow$	SSIM $\uparrow$	LPIPS $\downarrow$	FID $\downarrow$	IDA $\downarrow$	LMD $\downarrow$
400 ( $< t^*$ )	23.393	0.659	0.394	42.055	0.853	3.781
1000 ( $> t^*$ )	<u>24.172</u>	<u>0.657</u>	0.336	<b>14.556</b>	<u>0.761</u>	3.470
$t^*$ [690,925]	<b>24.349</b>	<b>0.664</b>	<b>0.332</b>	<u>14.780</u>	<b>0.748</b>	<b>3.419</b>

trained RM with various alternatives, including GAN-based GFP-GAN [22], CodeBook-based RestoreFormer [36] and deterministic-based SwinIR [25]. To ensure a fair comparison, we first fine-tune each RM on the FFHQ [17] dataset before integrating it into our framework.

As shown in Tab. 9 and visualized in Fig. 13, GFP-GAN suffers from poor realism (higher FID). Integrating our approach significantly improves the realism of GFP-GAN while maintaining competitive fidelity. Also, we find that RestoreFormer outperforms GFP-GAN in realism, and our method can further enhance RestoreFormer in terms of fidelity, structural integrity, PSNR and SSIM. Finally, SwinIR achieves the highest PSNR and SSIM but produces overly smooth images, compromising realism. Incorporating our method with SwinIR substantially reduces FID, balancing fidelity and realism. Overall, our method consistently improves realism across different RMs while maintaining competitive fidelity, achieving a more optimal trade-off between perceptual quality and fidelity.

### C. More Visualization

This section presents additional qualitative comparisons with state-of-the-art methods, including GPEN [40], GFP-GAN [22], RestoreFormer [36], CodeFormer [43], DiffBIR [26], DAEFR [33], PGDiff [38], DiffFace [41], DR2 [37] and 3Diffusion [27].

For the CelebA-Test dataset, Fig. 14 demonstrates that our DynFaceRestore not only produces reconstructions closer to the ground truth than competing methods but also offers superior perceptual quality. This highlights the balance between fidelity and perceptual quality in our approach.

For the three real-world datasets—LFW-Test [14], Wider-Test [43], and Webphoto-Test [22]—the results in Fig. 15, Fig. 16, and Fig. 17, respectively, highlight the advantages of DynFaceRestore. Specifically, our approach consistently generates more realistic facial details, such as hair strands and beards, while effectively preserving the global structure and local textures.

### D. Limitations

A major limitation of our proposed method is its computational complexity, as shown in Tab. 1 (main paper). This is primarily due to the optimization of kernel prediction and the incorporation of DM guidance at each step. The acceler-



Table 9. Differnet RM model comparisons to in CelebA-Test. The best and second performances are highlighted with **bold** and underline.

Type	Method	PSNR $\uparrow$	SSIM $\uparrow$	LPIPS $\downarrow$	FID $\downarrow$	IDA $\downarrow$	LMD $\downarrow$
GAN	GFP-GAN	22.841	0.620	0.355	23.860	0.822	4.793
	Ours + GFP-GAN	<b>23.867</b>	<b>0.649</b>	<b>0.340</b>	<b>15.943</b>	<b>0.772</b>	<b>3.654</b>
CodeBook	RestoreFormer	23.001	0.592	0.376	22.874	0.783	4.464
	Ours + RestoreFormer	<b>23.794</b>	<b>0.655</b>	<b>0.341</b>	<b>17.042</b>	<b>0.820</b>	<b>3.859</b>
Deterministic	SwinIR	<b>26.177</b>	<b>0.746</b>	0.377	61.209	<b>0.720</b>	<b>3.101</b>
	Ours + SwinIR	24.349	0.664	<b>0.332</b>	<b>14.78</b>	0.748	3.419

ation through DDIM [31] has yet to be explored. Therefore, reducing the denoising steps and selectively applying guidance to the critical step offers a promising research direction to address this challenge.

Additionally, as illustrated in Fig. 18, the DBLM module in our DynFaceRestore framework exhibits limitations when handling the complex degradation patterns observed in old photographs, such as incomplete restoration due to residual artifacts (Fig. 18 left) or geometric distortions (Fig. 18 right). These limitations result in difficulties during the subsequent DM sampling and guidance processes, leading to difficulties in accurately identifying regions that require fidelity preservation and refinement. As a result, the overall restoration quality is degraded. We attribute this issue to the training of the pre-trained restoration model, which fails to capture the diverse and severe degradations commonly observed in old photographs. A straightforward and effective solution to overcome these limitations is to replace the RM with more advanced restoration models.

Moreover, real-world images often exhibit spatially varying degradations, posing a significant challenge in perfectly addressing the kernel mismatch issue. Treating the entire image as uniformly degraded can lead to undesired artifacts, as shown in Fig. 19, which our proposed method has not yet effectively resolved. Addressing this issue is crucial for future research, and a direct approach is to divide regions and estimate degradations separately.

## References

- [1] Chaofeng Chen, Xiaoming Li, Lingbo Yang, Xianhui Lin, Lei Zhang, and Kwan-Yee K Wong. Progressive semantic-aware style transformation for blind face restoration. In *Proceedings of the IEEE/CVF conference on computer vision and pattern recognition*, pages 11896–11905, 2021. 1, 2
- [2] Yu Chen, Ying Tai, Xiaoming Liu, Chunhua Shen, and Jian Yang. Fsrnet: End-to-end learning face super-resolution with facial priors. In *Proceedings of the IEEE conference on computer vision and pattern recognition*, pages 2492–2501, 2018. 2
- [3] Zhengrui Chen, Liying Lu, Ziyang Yuan, Yiming Zhu, Yu Li, Chun Yuan, and Weihong Deng. Blind face restoration under extreme conditions: Leveraging 3d-2d prior fusion for superior structural and texture recovery. In *Proceedings of the AAAI Conference on Artificial Intelligence*, pages 1263–1271, 2024. 2
- [4] Hyungjin Chung, Jeongsol Kim, Michael T Mccann, Marc L Klasky, and Jong Chul Ye. Diffusion posterior sampling for general noisy inverse problems. *arXiv preprint arXiv:2209.14687*, 2022. 2, 3
- [5] Hyungjin Chung, Jeongsol Kim, Sehui Kim, and Jong Chul Ye. Parallel diffusion models of operator and image for blind inverse problems. In *Proceedings of the IEEE/CVF Conference on Computer Vision and Pattern Recognition*, pages 6059–6069, 2023. 1, 2, 3, 4
- [6] Jiankang Deng, Jia Guo, Niannan Xue, and Stefanos Zafeiriou. Arcface: Additive angular margin loss for deep face recognition. In *Proceedings of the IEEE/CVF conference on computer vision and pattern recognition*, pages 4690–4699, 2019. 7
- [7] Prafulla Dhariwal and Alexander Nichol. Diffusion models beat gans on image synthesis. *Advances in neural information processing systems*, 34:8780–8794, 2021. 7
- [8] Keyan Ding, Kede Ma, Shiqi Wang, and Eero P Simoncelli. Image quality assessment: Unifying structure and texture similarity. *IEEE transactions on pattern analysis and machine intelligence*, 44(5):2567–2581, 2020. 6, 11
- [9] Patrick Esser, Robin Rombach, and Bjorn Ommer. Taming transformers for high-resolution image synthesis. In *Proceedings of the IEEE/CVF conference on computer vision and pattern recognition*, pages 12873–12883, 2021. 2
- [10] Ben Fei, Zhaoyang Lyu, Liang Pan, Junzhe Zhang, Weidong Yang, Tianyue Luo, Bo Zhang, and Bo Dai. Generative diffusion prior for unified image restoration and enhancement. In *Proceedings of the IEEE/CVF Conference on Computer Vision and Pattern Recognition*, pages 9935–9946, 2023. 1, 2, 3
- [11] Yuchao Gu, Xintao Wang, Liangbin Xie, Chao Dong, Gen Li, Ying Shan, and Ming-Ming Cheng. Vqfr: Blind face restoration with vector-quantized dictionary and parallel decoder. In *European Conference on Computer Vision*, pages 126–143. Springer, 2022. 2
- [12] Martin Heusel, Hubert Ramsauer, Thomas Unterthiner, Bernhard Nessler, and Sepp Hochreiter. Gans trained by a two time-scale update rule converge to a local nash equilibrium. *Advances in neural information processing systems*, 30, 2017. 7
- [13] Jonathan Ho, Ajay Jain, and Pieter Abbeel. Denoising diffusion probabilistic models. *Advances in neural information processing systems*, 33:6840–6851, 2020. 1, 3

- [14] Gary B Huang, Marwan Mattar, Tamara Berg, and Eric Learned-Miller. Labeled faces in the wild: A database for studying face recognition in unconstrained environments. In *Workshop on faces in 'Real-Life' Images: detection, alignment, and recognition*, 2008. 7, 14
- [15] Björn Jawerth and Wim Sweldens. An overview of wavelet based multiresolution analyses. *SIAM review*, 36(3):377–412, 1994. 6, 11
- [16] Tero Karras. Progressive growing of gans for improved quality, stability, and variation. *arXiv preprint arXiv:1710.10196*, 2017. 7
- [17] Tero Karras, Samuli Laine, and Timo Aila. A style-based generator architecture for generative adversarial networks. In *Proceedings of the IEEE/CVF conference on computer vision and pattern recognition*, pages 4401–4410, 2019. 7, 14
- [18] Tero Karras, Samuli Laine, and Timo Aila. A style-based generator architecture for generative adversarial networks. In *Proceedings of the IEEE/CVF conference on computer vision and pattern recognition*, pages 4401–4410, 2019. 2
- [19] Tero Karras, Samuli Laine, Miika Aittala, Janne Hellsten, Jaakko Lehtinen, and Timo Aila. Analyzing and improving the image quality of stylegan. In *Proceedings of the IEEE/CVF conference on computer vision and pattern recognition*, pages 8110–8119, 2020. 2
- [20] Bahjat Kavar, Michael Elad, Stefano Ermon, and Jiaming Song. Denoising diffusion restoration models. *Advances in Neural Information Processing Systems*, 35:23593–23606, 2022. 3
- [21] Cansu Korkmaz, A Murat Tekalp, and Zafer Dogan. Training generative image super-resolution models by wavelet-domain losses enables better control of artifacts. In *Proceedings of the IEEE/CVF Conference on Computer Vision and Pattern Recognition*, pages 5926–5936, 2024. 6, 11
- [22] Ayushi Kumar and Avimanyou Vatsa. Influence of gfp gan on melanoma classification. In *2022 IEEE Integrated STEM Education Conference (ISEC)*, pages 334–339. IEEE, 2022. 1, 2, 7, 14
- [23] Charles Laroche, Andrés Almansa, and Eva Coupete. Fast diffusion em: a diffusion model for blind inverse problems with application to deconvolution. In *Proceedings of the IEEE/CVF Winter Conference on Applications of Computer Vision*, pages 5271–5281, 2024. 3
- [24] Wenjie Li, Mei Wang, Kai Zhang, Juncheng Li, Xiaoming Li, Yuhang Zhang, Guangwei Gao, Weihong Deng, and Chia-Wen Lin. Survey on deep face restoration: From non-blind to blind and beyond. *arXiv preprint arXiv:2309.15490*, 2023. 1
- [25] Jingyun Liang, Jiezhang Cao, Guolei Sun, Kai Zhang, Luc Van Gool, and Radu Timofte. Swinir: Image restoration using swin transformer. In *Proceedings of the IEEE/CVF international conference on computer vision*, pages 1833–1844, 2021. 4, 9, 14
- [26] Xinqi Lin, Jingwen He, Ziyang Chen, Zhaoyang Lyu, Bo Dai, Fanghua Yu, Yu Qiao, Wanli Ouyang, and Chao Dong. Diffbir: Toward blind image restoration with generative diffusion prior. In *European Conference on Computer Vision*, pages 430–448. Springer, 2024. 2, 3, 7, 14
- [27] Xiaobin Lu, Xiaobin Hu, Jun Luo, Ben Zhu, Yaping Ruan, and Wenqi Ren. 3d priors-guided diffusion for blind face restoration. In *Proceedings of the 32nd ACM International Conference on Multimedia*, pages 1829–1838, 2024. 2, 7, 14
- [28] Yunqi Miao, Jiankang Deng, and Jungong Han. Waveface: Authentic face restoration with efficient frequency recovery. In *Proceedings of the IEEE/CVF Conference on Computer Vision and Pattern Recognition*, pages 6583–6592, 2024. 2, 7, 9
- [29] Xinmin Qiu, Congying Han, Zicheng Zhang, Bonan Li, Tiande Guo, and Xuecheng Nie. Diffbfr: Bootstrapping diffusion model for blind face restoration. In *Proceedings of the 31st ACM International Conference on Multimedia*, pages 7785–7795, 2023. 2
- [30] Ziyi Shen, Wei-Sheng Lai, Tingfa Xu, Jan Kautz, and Ming-Hsuan Yang. Deep semantic face deblurring. In *Proceedings of the IEEE conference on computer vision and pattern recognition*, pages 8260–8269, 2018. 2
- [31] Jiaming Song, Chenlin Meng, and Stefano Ermon. Denoising diffusion implicit models. *arXiv preprint arXiv:2010.02502*, 2020. 15
- [32] Maitreya Suin, Nithin Gopalakrishnan Nair, Chun Pong Lau, Vishal M Patel, and Rama Chellappa. Diffuse and restore: A region-adaptive diffusion model for identity-preserving blind face restoration. In *Proceedings of the IEEE/CVF Winter Conference on Applications of Computer Vision*, pages 6343–6352, 2024. 2
- [33] Yu-Ju Tsai, Yu-Lun Liu, Lu Qi, Kelvin C. K. Chan, and Ming-Hsuan Yang. Dual associated encoder for face restoration, 2024. 2, 7, 14
- [34] Tao Wang, Kaihao Zhang, Xuanxi Chen, Wenhan Luo, Jiankang Deng, Tong Lu, Xiaochun Cao, Wei Liu, Hongdong Li, and Stefanos Zafeiriou. A survey of deep face restoration: Denoise, super-resolution, deblur, artifact removal. *arXiv preprint arXiv:2211.02831*, 2022. 1
- [35] Yinhuai Wang, Jiwen Yu, and Jian Zhang. Zero-shot image restoration using denoising diffusion null-space model. *arXiv preprint arXiv:2212.00490*, 2022. 3
- [36] Zhouxia Wang, Jiawei Zhang, Runjian Chen, Wenping Wang, and Ping Luo. Restoreformer: High-quality blind face restoration from undegraded key-value pairs. In *Proceedings of the IEEE/CVF conference on computer vision and pattern recognition*, pages 17512–17521, 2022. 2, 7, 14
- [37] Zhixin Wang, Ziyang Zhang, Xiaoyun Zhang, Huangjie Zheng, Mingyuan Zhou, Ya Zhang, and Yanfeng Wang. Dr2: Diffusion-based robust degradation remover for blind face restoration. In *Proceedings of the IEEE/CVF Conference on Computer Vision and Pattern Recognition*, pages 1704–1713, 2023. 2, 7, 14
- [38] Peiqing Yang, Shangchen Zhou, Qingyi Tao, and Chen Change Loy. Pgdif: Guiding diffusion models for versatile face restoration via partial guidance. *Advances in Neural Information Processing Systems*, 36, 2024. 1, 2, 3, 7, 14
- [39] Shuo Yang, Ping Luo, Chen-Change Loy, and Xiaoou Tang. Wider face: A face detection benchmark. In *Proceedings of the IEEE conference on computer vision and pattern recognition*, pages 5525–5533, 2016. 7

- [40] Tao Yang, Peiran Ren, Xuansong Xie, and Lei Zhang. Gan prior embedded network for blind face restoration in the wild. In *Proceedings of the IEEE/CVF conference on computer vision and pattern recognition*, pages 672–681, 2021. [1](#), [2](#), [7](#), [14](#)
- [41] Zongsheng Yue and Chen Change Loy. Diffface: Blind face restoration with diffused error contraction. *IEEE Transactions on Pattern Analysis and Machine Intelligence*, 2024. [1](#), [2](#), [7](#), [9](#), [14](#)
- [42] Richard Zhang, Phillip Isola, Alexei A Efros, Eli Shechtman, and Oliver Wang. The unreasonable effectiveness of deep features as a perceptual metric. In *Proceedings of the IEEE conference on computer vision and pattern recognition*, pages 586–595, 2018. [7](#)
- [43] Shangchen Zhou, Kelvin Chan, Chongyi Li, and Chen Change Loy. Towards robust blind face restoration with codebook lookup transformer. *Advances in Neural Information Processing Systems*, 35:30599–30611, 2022. [2](#), [7](#), [14](#)

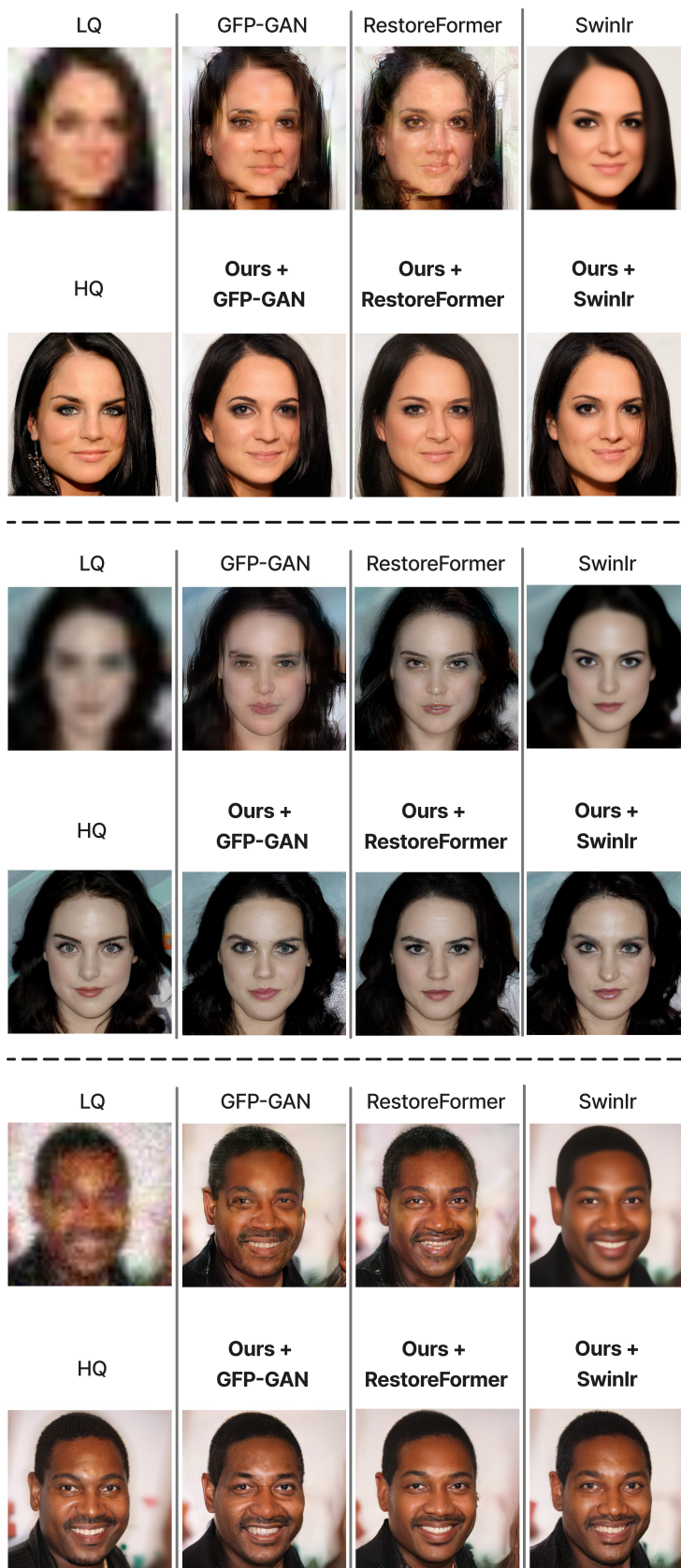


Figure 13. Ablation study with different RMs.



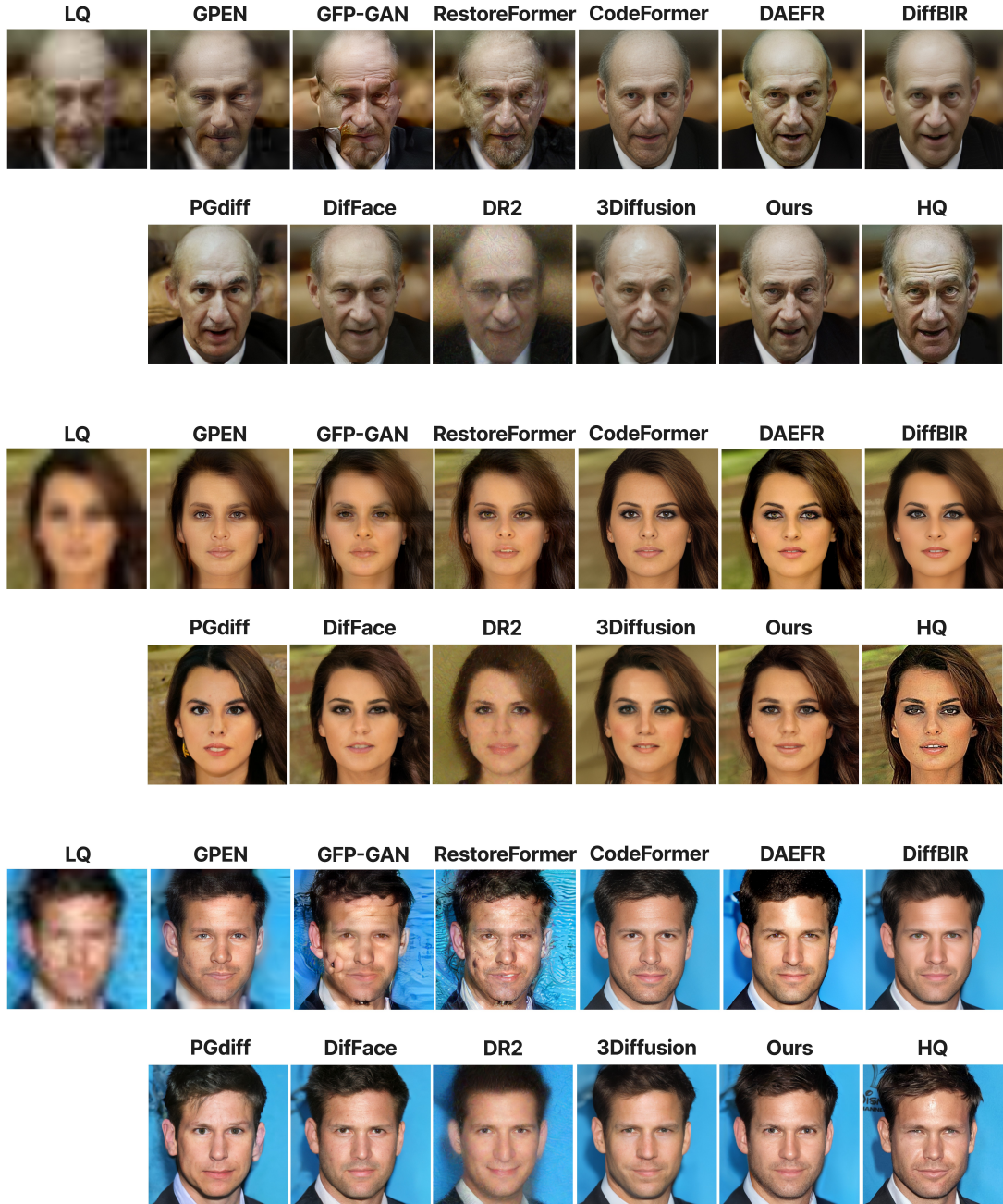


Figure 14. More visual comparisons on CelebA-Test. Our method achieves high-fidelity reconstructions while preserving natural facial features.

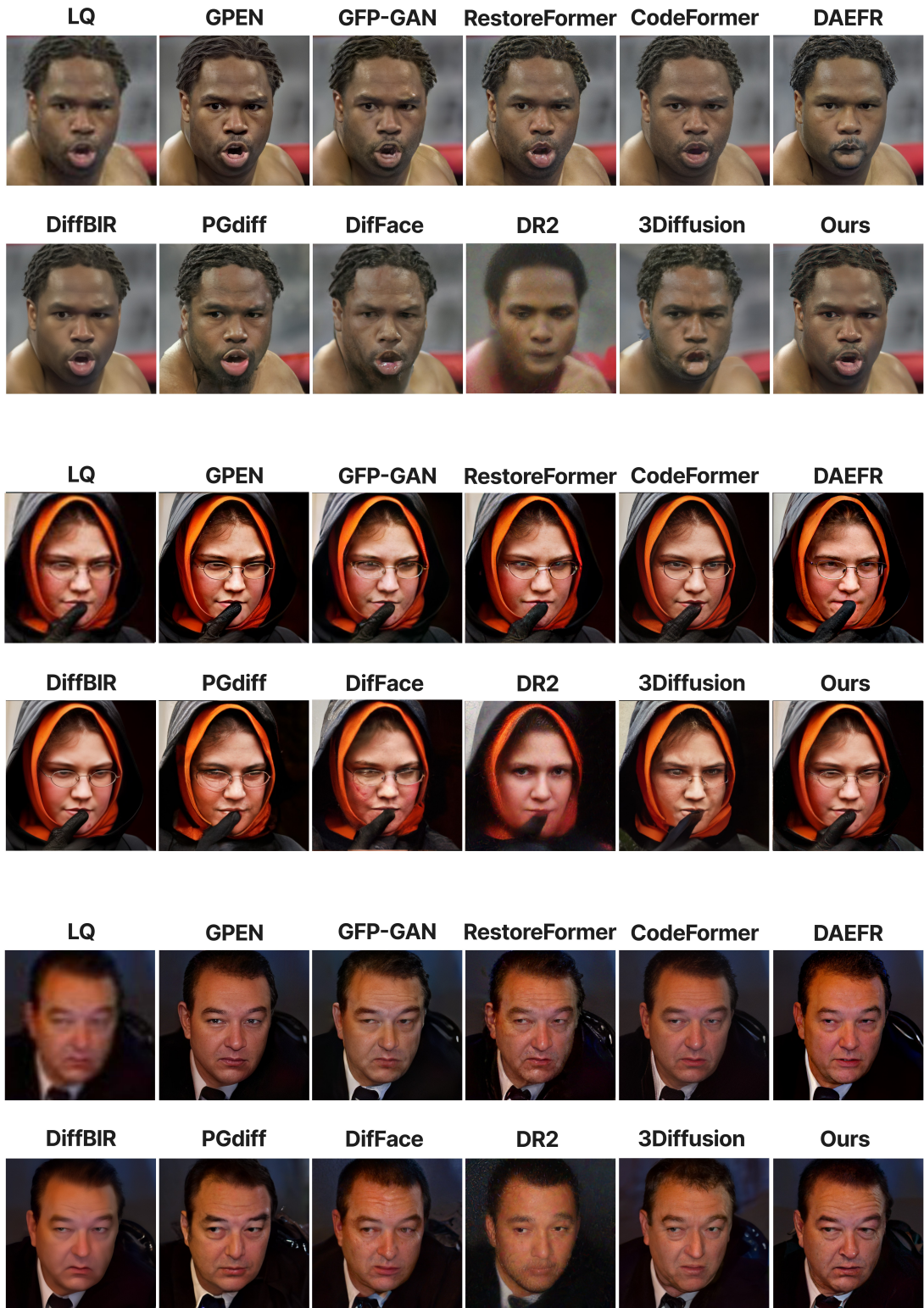


Figure 15. Qualitative results from LFW-Test demonstrate that our restoration method produces more natural features (e.g., eyes) and realistic details (e.g., hair) compared to other approaches, with improved fidelity.





Figure 16. More visual comparisons on Wider-Test. Our restoration method produces more natural features (e.g., eyes) and realistic details (e.g., hair, skin) compared to other approaches, with improved fidelity.

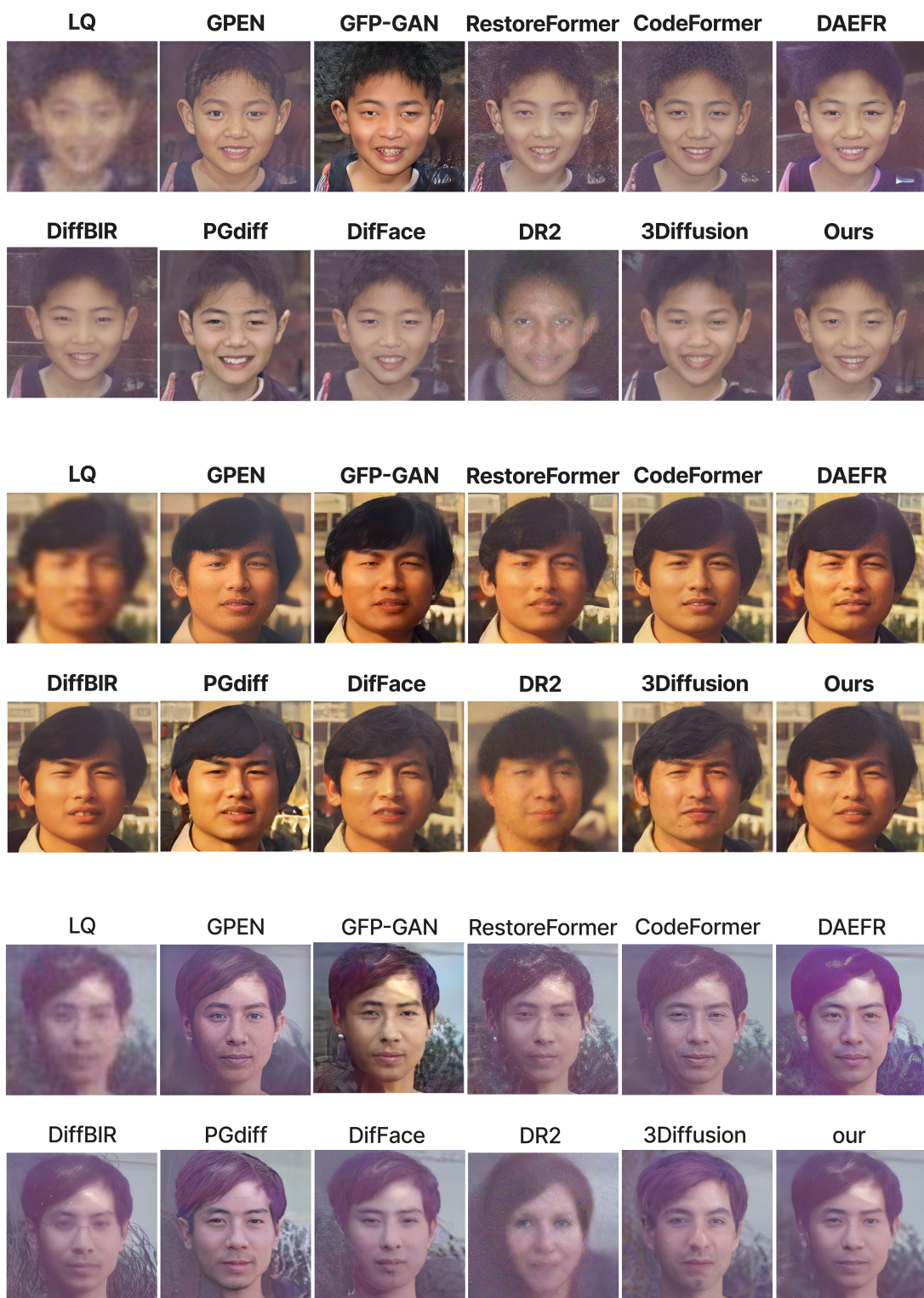


Figure 17. More visual comparisons on Webphoto-Test. Our restoration method produces more natural features (e.g., eyes) and realistic details (e.g., hair, skin) compared to other approaches, with improved fidelity.



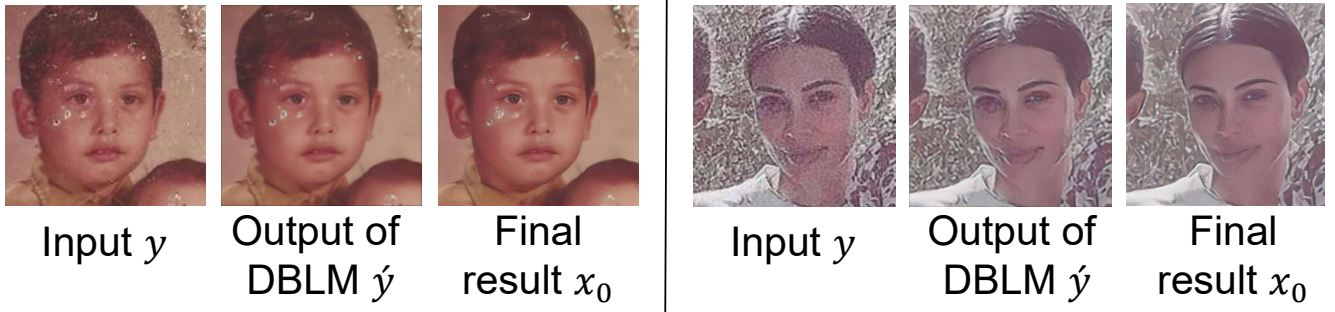


Figure 18. Limitations of Our DynFaceRestore. This issue likely arises from limitations in the degradation pipeline used to synthesize low-quality images for simulating real-world degradation. The current pipeline inadequately captures old photographs’ diverse and severe degradation characteristics. Revising the pipeline to represent these complexities better is essential for improving restoration performance in such challenging scenarios.



Figure 19. Limitations of Our DynFaceRestore. We degrade images using Eq. (18), applying both global degradation (uniformly across the entire image) and local degradation (independently for different small regions). The results indicate the appearance of artifacts in the mouth and eye regions.